Monthly Notices
of the
ROYAL ASTRONOMICAL SOCIETY

MNRAS **448,** 3248–3264 (2015) doi:10.1093/mnras/stv251

A detailed study of feedback from a massive star

Sam Geen,[1,2★] Joakim Rosdahl,[2,3] Jeremy Blaizot,[2] Julien Devriendt[2,4]
and Adrianne Slyz[4]

[1] *Laboratoire AIM, Paris-Saclay, CEA/IRFU/SAp - CNRS - Université Paris Diderot, F-91191 Gif-sur-Yvette Cedex, France*
[2] *CRAL, Université de Lyon I, CNRS UMR 5574, ENS-Lyon, 9 avenue Charles André, F-69561 Saint-Genis-Laval, France*
[3] *Leiden Observatory, Leiden University, PO Box 9513, NL-2300 RA Leiden, the Netherlands*
[4] *University of Oxford, Astrophysics, Keble Road, Oxford OX1 3RH, UK*

Accepted 2015 February 5. Received 2015 February 3; in original form 2014 November 12

ABSTRACT

We present numerical simulations of a 15 $M_\odot$ star in a suite of idealized environments in order to quantify the amount of energy transmitted to the interstellar medium (ISM). We include models of stellar winds, UV photoionization and the subsequent supernova based on theoretical models and observations of stellar evolution. The system is simulated in 3D using RAMSES-RT, an Adaptive Mesh Refinement Radiation Hydrodynamics code. We find that stellar winds have a negligible impact on the system owing to their relatively low luminosity compared to the other processes. The main impact of photoionization is to reduce the density of the medium into which the supernova explodes, reducing the rate of radiative cooling of the subsequent supernova. Finally, we present a grid of models quantifying the energy and momentum of the system that can be used to motivate simulations of feedback in the ISM unable to fully resolve the processes discussed in this work.

Key words: methods: numerical – stars: massive – supernovae: general – H II regions – ISM: supernova remnants.

1 INTRODUCTION

The ΛCDM (Cosmological Constant Λ + Cold Dark Matter) model of cosmological galaxy formation has achieved great successes in explaining the large-scale structure of the universe. However, problems remain with this model that must be addressed before we can match completely our theoretical models with observations. One key issue is that the stellar masses of galaxies observed in the universe are lower than what would be expected if each galaxy were embedded in a dark matter halo with a constant luminosity–halo mass proportion. Similarly, large-scale mass outflows from galaxies have been observed (see review by Veilleux, Cecil & Bland-Hawthorn 2005). In both cases, stellar feedback, particularly from supernovae, but also from stellar photoionization and winds, has been employed with varying success to explain this discrepancy.[1] Simple analytical and semi-analytical models (SAMs; analytical models run in a framework of pure dark matter cosmological *N*-body simulations) have found that the energy from stellar sources is sufficient to launch galactic winds and suppress star formation in lower mass haloes (Benson et al. 2003).

Despite the success of recent models in explaining many of the observed properties of galaxies, hydrodynamical numerical simulations of galaxy formation have encountered difficulties in reproducing these results in more self-consistent settings. Scannapieco et al. (2012) find that there is still significant disagreement between analytical models, SAMs, and hydrodynamic simulations, both smoothed particle hydrodynamics and adaptive mesh refinement (AMR) simulations. A large part of this problem is the limitation imposed by numerical resolution. If adequate numerical resolution is not achieved, the gas will cool radiatively before it has a chance to add momentum to the interstellar medium (ISM). Gerritsen & Icke (1997) address this problem by enforcing thermal equilibrium for gas particles with a cooling time of less than 10 per cent of the current timestep. Hopkins et al. (2013) propose instead to deposit the supernova blast on to the grid as momentum if the grid resolution is below the cooling length as calculated by Cox (1972), using values for momentum calibrated elsewhere. A similar method has been implemented by Kimm & Cen (2014). Iffrig & Hennebelle (2014) find that the momentum added to the ISM can be well approximated by taking the momentum of a Sedov blastwave (Sedov 1946) at the cooling time given by Cox (1972).

A major problem faced by numerical simulations of galaxy formation is to understand how this energy created by stars accounts for the observed properties of gas in the ISM and galactic outflows. This problem is complicated by the fact that the ISM is a

---

★ E-mail: samuel.geen@cea.fr

[1] Stellar feedback refers to the ability of stellar evolution processes to regulate the subsequent star formation rate.

Published by Oxford University Press on behalf of the Royal Astronomical Society

multiphase medium that much be simulated with resolutions on the scale of parsecs or below if we wish to capture it without resorting to sub-grid modelling (a sub-grid model is an expression implemented in the code to account for processes that cannot be spatially resolved by the simulation). The densest phase is the cold neutral medium (CNM), made up of clouds and filaments at around 100 K. These are embedded in a warm, diffuse phase at around 10^4 K called the warm neutral medium if neutral or warm ionized medium if ionized by UV radiation. A hot ionized medium at above 10^6 K exists in bubbles formed by supernova explosions. As proposed in the results of analytical models by McKee & Ostriker (1977), the presence of these phases is thought to be the result of multiple supernova explosions. Springel & Hernquist (2003) and Murante et al. (2010) attempt to circumvent the limitations of resolution in their simulations with a 'sub-grid' model for the interaction between the cold and hot gas phases that are traced separately inside each fluid element. Springel & Hernquist (2003) also invoke winds phenomenologically to allow the escape of hot gas from the galaxy without resolving the evolution of supernova remnants in the ISM. Meanwhile, Navarro & White (1993) and Mihos & Hernquist (1994) model stellar feedback using kinetic winds. Dubois & Teyssier (2008) account for a lack of resolution by imposing a Sedov profile on to the gas when a supernova occurs.

The lifetime of an OB star is of the order of 10 Myr. The precise age depends on a number of factors such as mass, chemical composition and rotation velocity, as well as multiplicity, i.e. interactions with a companion star or stellar remnant. For the purposes of this paper, we ignore binary supernovae such as Type Ia, since the lifetimes of their progenitors are much longer and as such do not induce such immediate feedback into the ISM as single-star Type II supernovae, though ultimately their energy contribution may be important. Heger et al. (2003) state that stars must be over 8–10 $M_{\odot}$ to explode as supernovae. Further, they argue that above around 25 $M_{\odot}$ the type of supernova depends on the mass and metallicity, with very massive low-metallicity stars undergoing direct collapse to a black hole, many with a weak or no supernova. As stars of lower masses are more common according to the standard IMFs proposed by Salpeter (1955), Chabrier (2003) and Kroupa & Weidner (2003), the energy budget from supernovae of stars above 25 $M_{\odot}$ must be less than that of stars between 9 and 25 $M_{\odot}$. Supernovae at the lower end of this range release approximately 10^{51} erg as kinetic energy into the circumstellar medium (CSM; Chevalier 1977), though Nomoto et al. (2003) suggest that more massive stars exploding as hypernovae can release up to around 50 times this value, noting that, depending on its composition and evolution, a star above 25 $M_{\odot}$ can also produce a faint (below 10^{51} erg) supernova.

Estimates based on 1D simulations in a uniform medium suggest that only 3 to 10 per cent of the 10^{51} erg of kinetic energy produced by a supernova is transferred to the ISM depending on the physics modelled and the density of the external medium, and the remaining energy is lost to thermal radiation (Chevalier 1974; Spitzer 1978). Initially, once the shock has broken out of the star, it evolves adiabatically according to the Sedov–Taylor solution (Sedov 1946). Once the supernova remnant's thermal energy falls below its kinetic energy, it enters a pressure-driven snowplough phase. At this point, the pressure force from the hot, diffuse gas inside the remnant drops so that it is comparable to the deceleration from the accretion of matter from the external medium by the cold, dense shell surrounding the remnant. As the thermal pressure inside the remnant drops further, it enters a momentum-conserving snowplough phase. Eventually, the remnant is disrupted and destroyed when it merges with the turbulent ISM surrounding it. Cioffi, McKee & Bertschinger (1988) produce analytic empirically-motivated models of the evolution of a supernova remnant and estimate this merging time, which can in certain circumstances happen before the momentum-conserving phase is reached. A parametrized study of a single supernova in various uniform media was performed by Thornton et al. (1998), who find that while a remnant cools faster when the supernova explodes in a denser medium, the resulting kinetic energy in the dense shell is remarkably constant with the external medium's density and metallicity. Highly diffuse media can produce highly adiabatic shocks (Tang & Wang 2005), whilst very dense media produce supernova remnants that become momentum-conserving almost immediately (Tenorio-Tagle et al. 1991). More recently, Martizzi, Faucher-Giguère & Quataert (2014) and Iffrig & Hennebelle (2014) have studied isolated supernovae in multiphase environments in an attempt to address this issue. A further question is whether massive stars explode in dense clouds at all. Slyz et al. (2005) argue that the delay between star formation and the first supernova (given by the lifetime of massive stars as discussed above) enhances the multiphase ISM and star formation rates by allowing massive stars to drift out of star-forming clouds into lower density regions before exploding. Ceverino & Klypin (2009), Kimm & Cen (2014) and Hennebelle & Iffrig (2014) find that 'runaway stars' can drastically reduce energy loss rates from supernovae, produce more realistic galaxy bulge masses and increase the escape fraction of UV photons, since the supernovae now explode outside dense star-forming environments.

The impact of pre-supernova stellar feedback can also play a role in injecting energy into the ISM and modifying the environment into which supernovae explode. Star formation occurs in the CNM, where the gas is Jeans-unstable and collapses to form star-forming cores in molecular clouds. Stars feed back into this environment via three main processes – UV photoionization, stellar winds and protostellar jets. Early work by Strömgren (1939), Kahn (1954) and Oort & Spitzer (1955) argues that radiation feedback by UV photons emitted by OB stars plays an important role in regulating star formation in clouds. These photons heat the gas in clouds to around 10^4 K, preventing further star formation and drive thermal shocks that expel gas from the clouds. This is explored in simulations by Dale et al. (2005), Arthur et al. (2011), Walch et al. (2012, 2013), Dale et al. (2014), and the observations of, e.g. Chu & Kennicutt (1994), Redman et al. (2003). On a smaller scale, Bate (2012) argue that radiation feedback plays an important role in regulating the formation of star-forming cores and hence the shape of the initial mass function (IMF).

Krumholz & Matzner (2009) propose that radiation pressure may play a role in driving feedback from OB stars. However, we do not consider radiation pressure in this work. Krumholz & Thompson (2012), Sales et al. (2014) and Rosdahl et al. (in preparation) conclude that the impact of radiation pressure compared to that of UV photoheating is limited, though there may be regimes in which it becomes important.

Castor, Weaver & McCray (1975), Avedisova (1972) and Weaver et al. (1977) produce analytic expressions for the evolution of stellar wind-driven bubbles in the adiabatic regime. Unlike ionization fronts, which produce shocks via thermal differences between the ionized and neutral gas, stellar winds produce shocks via the interaction of winds travelling of the order of the escape velocity of the star (Kudritzki & Puls 2000) and the CSM. The balance of available energy from either process depends on the properties of the star. Higher metallicity stars are more opaque, and thus have lower luminosities whilst driving stronger stellar winds, whilst low-mass stars may not produce enough UV photons to ionize the surrounding medium. Recent work by Dale et al. (2014) has explored the relative impact of winds and photoionization from young star clusters on molecular cloud evolution. Working on larger scales, Agertz et al. (2013) produces a sub-grid model for galaxy formation simulations that gives the energy produced by each feedback process from a population of stars. Jets from protostars could also help explain low star formation efficiencies in star-forming clouds. See the review by Krumholz (2014) for more on this subject. These are mainly of importance in young clusters with active star formation, and as such will be implemented in future work studying feedback in these environments.

Considerable work has been carried out already on the evolution of supernovae inside circumstellar media previously modified by stellar winds and photoionization. Indeed, diverse structures in supernova remnants have been attributed to the existing density structure of the CSM, which is often created by the supernova progenitor prior to the explosion. Dwarkadas (2007) uses numerical simulations to explain observed structures in supernova remnants by invoking a Wolf–Rayet wind prior to the supernova, while Walch & Naab (2014) discuss the interaction between a pre-existing photoionized cloud and a supernova explosion. Pre-supernova stellar feedback can also alter the geometry of the supernova remnant. Garcia-Segura et al. (1999) note that stellar rotation can induce a bipolar structure in the wind-blown CSM. van Marle et al. (2008) argue that stellar rotation causes the density profile of the CSM to diverge from a Chevalier (1982) power law. Tenorio-Tagle et al. (1990) and Rozyczka et al. (1993) suggest that stellar motion with respect to the ISM gas can produce barrel-shaped supernova remnants as pre-supernova winds carve out a tube-like structure in the ISM, while Mackey et al. (2015) explore the interaction between the wind and ionization front in the context of a star moving with respect to the CSM. Supernova shocks are subject to turbulence driven by Rayleigh–Taylor, Vishniac and, in the case of non-spherical shocks, Kelvin–Helmholtz instabilties. Gull (1973) propose that these instabilities can modify the energetics of a supernova shock by converting kinetic energy on the shock into thermal energy via the turbulent energy cascade. Numerical simulations by Dwarkadas (2007), Fraschetti et al. (2010) report the growth of these instabilities. Ntormousi et al. (2011) and Krause et al. (2012) find that stellar wind shock fronts are also unstable, and determine that wind-blown bubbles will be prone to Vishniac instabilities, which grow due to radiative cooling and self-gravity (not included in our simulations; Vishniac 1983, 1994). By contrast, Ricotti (2014) argue that ionization fronts are not typically turbulent.

The role of this paper is to update the work of Thornton et al. (1998) by taking into account the role of photoionization and stellar winds from a single 15 $\mathrm{M}_{\odot}$ star on the evolution of its subsequent supernova remnant in a set of uniform media of various densities and metallicities. In addition to this, we take advantage of advances in computing to run 3D, rather than spherically-symmetric 1D simulations as in, e.g. Chevalier (1974), Cioffi et al. (1988) and Thornton et al. (1998). The advantage of using 3D simulations as opposed to 1D simulations is that we are able to quantify the impact of these instabilities on the energetics of the supernova. We resolve the gas to sub-parsec resolutions such that our results converge in test runs (see Section 2.2).

Our paper is organized as follows. Section 2 is concerned with the models used for stellar winds, photoionization and supernova feedback, as well as the setup of the numerical simulations. In Section 3, we present in detail one of our simulations in order to give a qualitative description of the structures formed by the star. We then look at the response of two sample environments to winds and photoionization by studying each process in isolation. Section 4 discusses how including each of the processes affects the energy and momentum transferred to media at various densities and metallicites. Finally, we discuss our results and some possible limitations in light of simplifications made by the study.

2 METHODS

2.1 A model star

In our simulations, we simulate a single 15 $\mathrm{M}_{\odot}$ star in a variety of environments. The stellar wind model implemented in this paper is taken from the Padova stellar evolution models (Marigo et al. 2008). The initial velocity of the wind is set to the escape velocity of the star. Kudritzki & Puls (2000) find that wind velocities only noticeably exceed the escape velocity for star more massive than the one modelled in this paper. The temperature of the gas ejected is taken to be the surface temperature of the star. While Runacres & Owocki (2005) argue that the temperature decreases rapidly once it leaves the star, the kinetic energy of the wind dominates by roughly three orders of magnitude and thus the precise temperature of the wind is unimportant. For the metallicity of the wind, we assume a surface metallicity for our star equal to that of the external medium for all simulations. The lifetime of the star is allowed to vary with metallicity as per the Marigo et al. (2008) model. Based on the same model, the lifetime of the star is set to 13.2 Myr for a star of $\mathrm{Z}_{\odot}$ and 15.8 Myr for a star of 0.1 $\mathrm{Z}_{\odot}$, where $\mathrm{Z}_{\odot}$ is the solar metal mass fraction, set to a fiducial value of 0.02 in absolute units. For runs including the radiative transfer of ionizing photons, we produce a set of metallicity and age-dependent spectra for a 15 $\mathrm{M}_{\odot}$ star using the STARBURST99 web-based software and data package (Leitherer et al. 1999). Once the star has reached the end of its lifetime, it explodes as a supernova. We use a supernova energy of 1.2×10^{51} erg and a remnant mass of 1.5 $\mathrm{M}_{\odot}$ as per Kovetz, Yaron & Prialnik (2009) and Smartt et al. (2009). A metallicity of 6.5 $\mathrm{Z}_{\odot}$ is used for the gas ejected by the supernova explosion, which we derive from the results of Chieffi & Limongi (2013). Values for cumulative energy and mass input from the star as winds, ionizing photons and supernova explosions are given in Fig. 1. It is worth noting that the total energy emitted in ionizing photons exceeds the supernova energy. However, it is not guaranteed that all of this energy will couple with the surrounding gas as a kinetic shock. The energy in ionizing photons from the 0.1 $\mathrm{Z}_{\odot}$ star is higher than that of the $\mathrm{Z}_{\odot}$ star owing to the lower opacity of the former. The energy in ionizing photons decreases slowly over the lifetime of the star as it expands and its surface temperature drops. The total energy available from stellar winds for this star is roughly three orders of magnitude lower than the supernova energy. Winds from more metal-rich stars eject proportionally more mass at higher velocities than more metal-poor stars, again due to the higher opacity that allows greater coupling of photons to the surface ions of the star.

We run this stellar model in a variety of uniform media with different initial densities and metallicities. Details of these simulations are given Section 2.2. The star is positioned at the centre of the simulation volume, and is static with respect to the external medium. The wind is imposed on the grid by incrementing the density, momentum and thermal energy of the grid cells inside a sphere of radius 20 cells at the highest refinement level with an inverse-square distribution to give a consistent mass in each spherical shell. We use a sphere to impose the solution rather than a single point in order to attempt to minimize the effect of grid artefacts and produce a spherically-shaped wind (note also that momentum cannot be deposited on to the grid in a spherical configuration in a single cell, since the velocity vectors would cancel each other). For the weak wind early in the star's lifetime, we find that some grid artefacts are unavoidable. This is discussed further in Section 3.1. The supernova energy and mass is deposited as a thermal pulse at the centre of the grid. Photons, likewise, are deposited on to the centre of the grid and evolve subsequently according to the prescription described in Rosdahl et al. (2013).

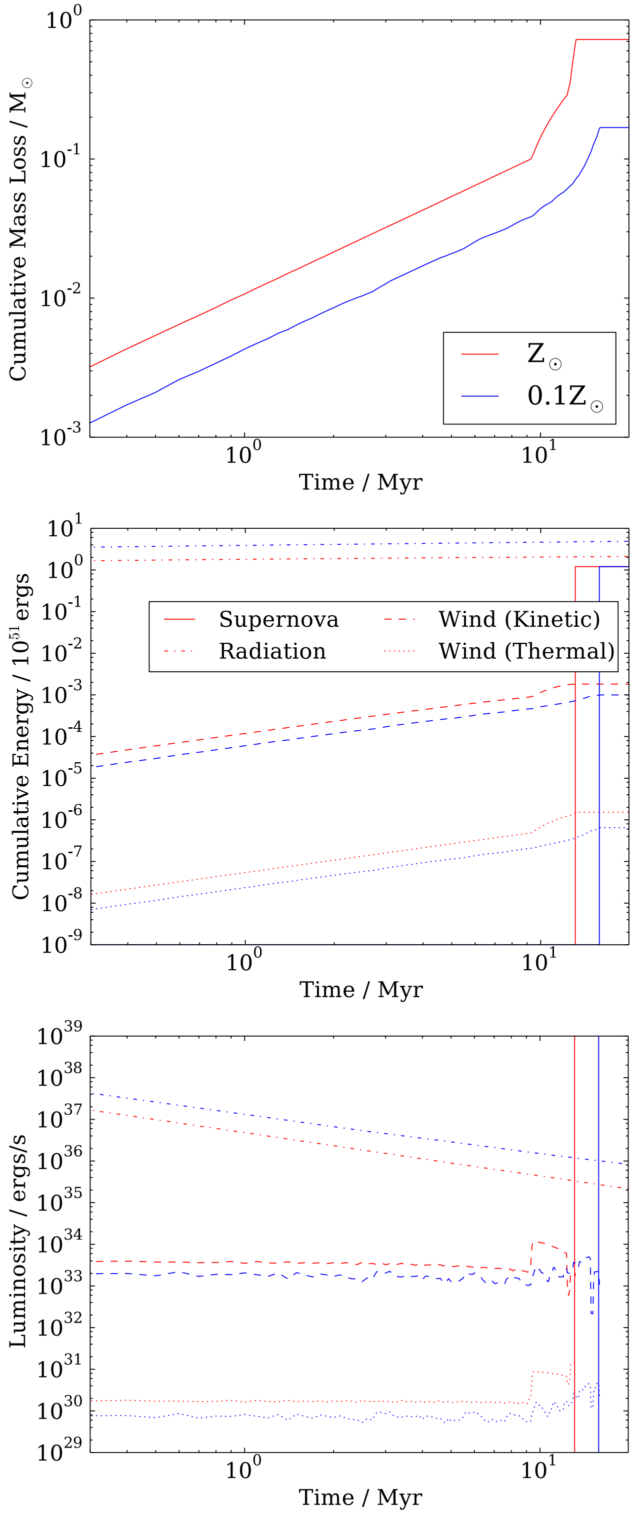

Figure 1. Cumulative mass-loss (top), cumulative energy output (middle) and energy output rate (bottom) against time from a 15 $M_\odot$ star of metallicities $Z_\odot$ in red and 0.1 $Z_\odot$ in blue, where $Z_\odot$ is a fiducial solar metal mass fraction, equivalent to 0.02 in absolute units. For the lower two figures, supernova energy is shown as a solid line, wind kinetic energy as a dashed line, wind thermal energy as a dotted line and the energy in ionizing photons as a dot–dashed line. The line marked 'radiation' is the total energy in photons emitted from the star above the ionization energy of hydrogen. See Section 2.1 for a full description of the values used.

2.2 Numerical simulations

We run our simulations using RAMSES-RT (Rosdahl et al. 2013), a radiation hydrodynamics (RHD) extension of the AMR code RAMSES (Teyssier 2002), which includes the propagation of photons and their on-the-fly interaction with gas via photoionization and heating of hydrogen and helium. The advection of photons between grid cells is described with a first-order moment method and the set of radiation transport equations is closed with the M1 relation for the Eddington tensor. RAMSES-RT solves the non-equilibrium evolution of the ionization fractions of hydrogen and helium, along with ionizing photon fluxes and the gas temperature in each grid cell. Metal cooling is added assuming photoionization equilibrium with a Haardt & Madau (1996) redshift 0 UV background. The spectrum of ionizing photons from the star is modelled by three photon groups, bracketed by the ionization energies of H I, He I and He II. We ignore photons at sub-ionizing energies, and we ignore radiation–dust interactions. As stated in the Introduction, we also ignore radiation pressure. Rosdahl et al (in preparation) discusses direct radiation pressure from photoionization in similar simulation setups and find it to be negligible compared to the effect of photoionization heating.

The simulations we ran are listed in Table 1. In the runs where the medium around the star has a number density of 0.1 and 30 atoms cm^{-3} at solar metallicity, we perform a series of experiments in which different stellar processes are included (namely stellar winds, photoionization and supernova feedback), in order to investigate the relative impact of each feedback process in isolation. These densities are selected as they represent roughly the densities found in the diffuse and dense phases of the ISM. 0.1 atoms cm^{-3} is also a point of comparison for previous works. We then run a grid of simulations with every physical process included at five different densities around these values, at both solar and 10 per cent of solar metallicity. For each simulation, we run a low-resolution equivalent at the given initial density and metallicity and allow the temperature to relax to an equilibrium value. We then set the initial temperature to this value. To simplify the model and allow us to study the impact of the model star in a controlled environment, we do not include external sources of heating or turbulence. This will be explored in future works, though Raga, Canto & Rodriguez (2012) and Tremblin et al. (2014) produce 1D models for H II regions in the presence of turbulence. Using Cioffi et al. (1988), we calculate that the supernova remnant will merge with the ISM due to turbulence on time-scales of around 20 Myr at 100 atoms cm^{-3} and 70 Myr at 0.1 atoms cm^{-3}, several times longer than the time over which we follow the supernova remnant. We do not consider self-gravity in this work, since the structures produced in this work are more or less spherically symmetric and as such are not strongly self-gravitating. In a more realistic medium, the external density field will dominate the gravitational field in the CSM and subsequent supernova remnant.

Each simulation is run in a cubic box with length 4.8 kpc and a root grid with 64^3 cells. The large box size was originally chosen in order to limit artefacts arising from the Poisson solver in RAMSES,

Table 1. Table of properties of numerical simulations included in this paper. $n_{\mathrm{H,ini}}$, T_{ini} and Z_{ini} refer to the initial hydrogen number density, initial temperature and initial metallicity of the simulation volume around the star (we determine T_{ini} by allowing a low-resolution volume with the same density and metallicity to relax to a given temperature, and then set the initial temperature of the simulation to this value). ‘N’ refers to the initial hydrogen number density, given by the number after it. ‘Z’ denotes the initial metallicity, which is either ‘solar’ ($Z = Z_{\odot}$) given by ‘so’, or ‘low’ ($Z = 0.1\,Z_{\odot}$) given by ‘lo’. Letters ‘S’, ‘W’ and ‘R’ denote that a supernova (SNe), stellar winds and radiation hydrodynamics (RHD) respectively, are included in the simulation. See Section 2.2 for full details of the simulations run.

Name	$n_{\mathrm{H,ini}}$/atoms cm^{-3}	T_{ini}/K	$Z_{\mathrm{ini}}/Z_{\odot}$	SNe?	Winds?	RHD?
N0.1ZsoS	0.1	62	1.0	✓		
N0.1ZsoSW	0.1	62	1.0	✓	✓	
N0.1ZsoSR	0.1	62	1.0	✓		✓
N0.1ZsoSWR	0.1	62	1.0	✓	✓	✓
N0.1ZloSWR	0.1	94	0.1	✓	✓	✓
N0.5ZsoSWR	0.5	31	1.0	✓	✓	✓
N0.5ZloSWR	0.5	75	0.1	✓	✓	✓
N5ZsoSWR	5	12	1.0	✓	✓	✓
N5ZloSWR	5	32	0.1	✓	✓	✓
N30ZsoS	30	8.2	1.0	✓		
N30ZsoSW	30	8.2	1.0	✓	✓	
N30ZsoSR	30	8.2	1.0	✓		✓
N30ZsoSWR	30	8.2	1.0	✓	✓	✓
N30ZloSWR	30	13	0.1	✓	✓	✓
N100ZsoSWR	100	8.2	1.0	✓	✓	✓
N100ZloSWR	100	9.9	0.1	✓	✓	✓

which uses periodic boundary conditions, though we found that self-gravity had a limited effect on the results and did not include it in the final runs. We then allow the simulations to refine up to a maximum spatial resolution of 0.6 pc, 2^{-13} of the box length. A cell is allowed to refine if the fractional difference in either pressure or density with a neighbouring cell exceeds 0.2 (though tests conclude that results do not vary significantly if this threshold is varied). We calibrate the choice of maximum spatial resolution based on tests of the N0.1ZsoSW, N30ZsoSW and N30ZsoSR simulations. The spatial resolution was selected such that the evolution of energy and shock radius in the simulation was unchanged to within a few per cent by a factor of 2 decrease in grid cell size. The only exception is the N30ZsoS simulation, which has a short cooling time for the spatial resolution. Here, we use an extra level of refinement, corresponding to 0.3 pc maximum spatial resolution, although the difference between this and a run taken at the default resolution is small.

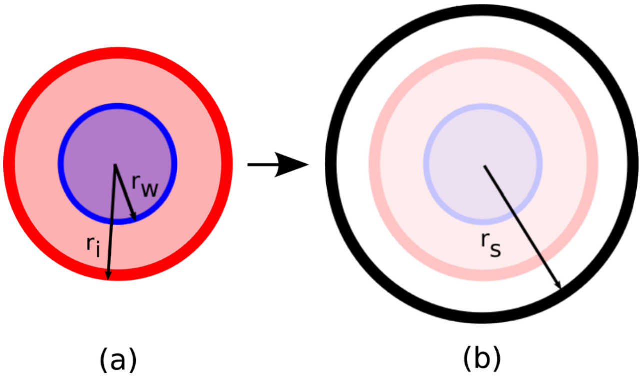

Figure 2. A schematic drawing of the structures around the star before and after the supernova event. Each process creates a heated underdensity surrounded by an overdense shell. Left: the CSM just before the supernova. The ionized gas forms a shell to radius r_{i}. Inside r_{i} is the wind-blown cavity with its own (typically weak) shell at r_{w}. Around the star is a small free-streaming radius, where the wind has yet to shock against the CSM gas (cf. Weaver et al. 1977). Right: the CSM after the supernova. The supernova sweeps up and destroys the existing structures in the CSM and creates its own hot, diffuse bubble and a dense shell of radius r_{s} that spreads into the ISM (pre-existing structures overlaid for comparison).

3 EVOLUTION OF THE CSM

3.1 Overview

The structures produced by the star in the CSM are broadly similar for all runs, though the precise properties vary for each run. A schematic view is given in Fig. 2. As the star evolves, an ionization front at r_{i} expands outwards, bounded by a dense shell of swept-up material, with a wind-driven bubble at r_{w} embedded inside it. Then, once the star explodes as a supernova, a supernova-driven shock propagates outwards at r_{s}, erasing the previous structures, interacting with the shell of the ionization front and propagating into the unshocked ISM. Radial profiles for each run containing both stellar winds and RHD are shown in Figs 3 and 4. The gas inside the ionization front ($r < r_{\mathrm{i}}$) reaches a temperature of around 10^4 K inside a sphere of radius r_{i}, where r_{i} is the radius of the ionization front (neglecting the thickness of the shell at r_{i}). The precise temperature found in observed H II regions varies between 5000 and 15 000 K as a function of gas density and metallicity (Draine 2011), but for the purposes of this work we use 10^4 K in our analysis since it matches our solar metallicity results well. At first the gas expands hydrostatically to the Strömgren radius, the radius at which the number of recombinations equals the number of photoionizations. The pressure difference between the ionized gas and its surroundings causes the gas to expand outwards into the neutral ISM. As it does so, it creates an overdense shell at r_{i}, gathering matter from

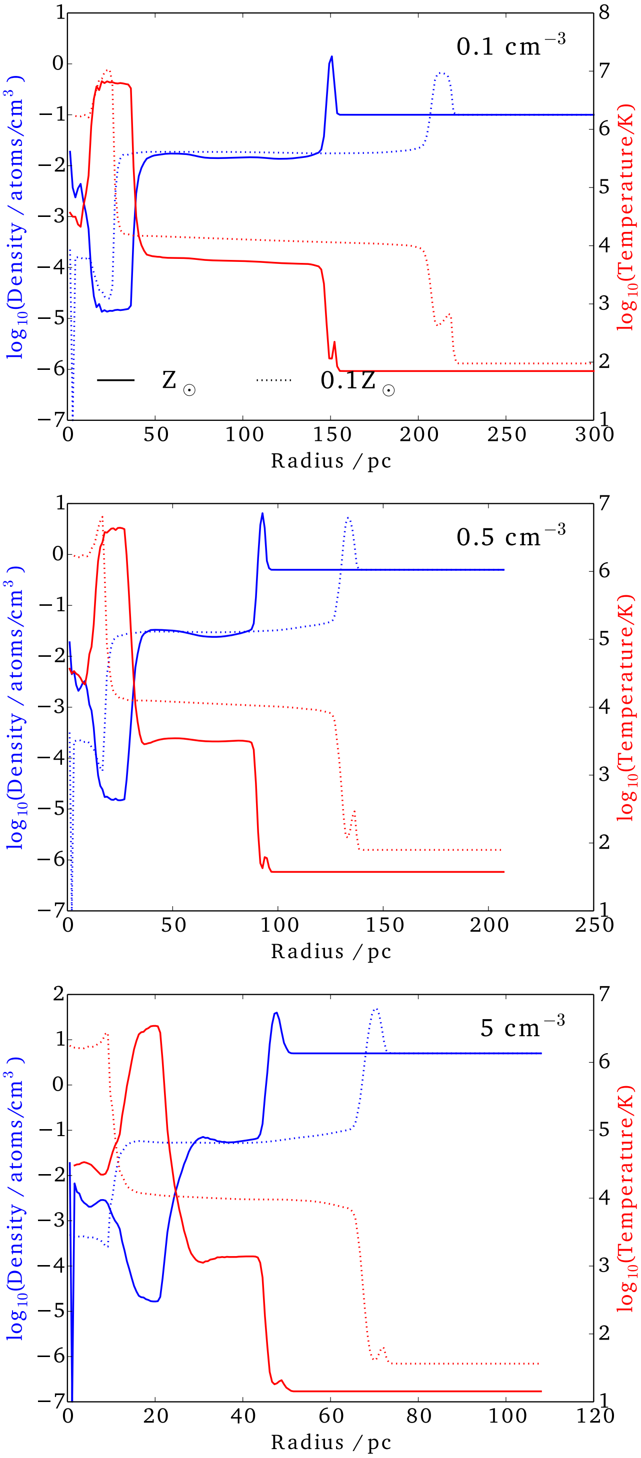

Figure 3. Density and temperature radial profiles at $t_{\rm SN}$ plotted for each of the runs containing both winds and photoionization, comparing solar to 10 per cent solar metallicity simulations. Density is shown in blue and temperature in red. A solid line indicates solar metallicity and a dotted line 0.1 Z$_\odot$. N0.1ZsoSWR and N0.1ZloSWR are plotted on the top row, N0.5ZsoSWR and N0.5ZloSWR on the middle row and N5ZsoSWR and N5ZloSWR on the bottom row. The other runs are plotted in Fig. 4. The value of $t_{\rm SN}$ used depends on the metallicity of the star in the simulation, as given in section 2.1. The value in each radial bin is found by averaging the values for all points inside that bin.

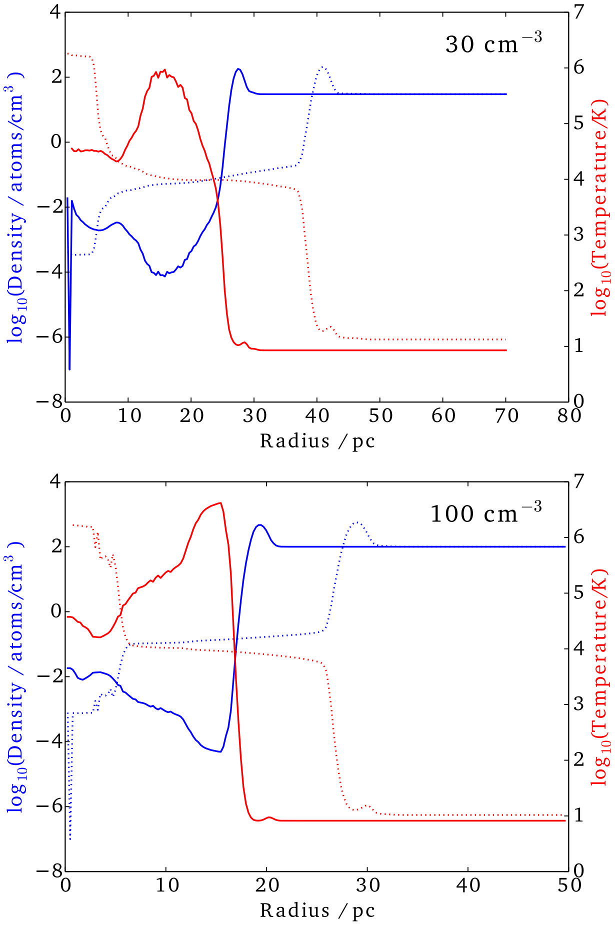

Figure 4. As in Fig. 3, but for the runs N30ZsoSWR and N30ZloSWR (top), and N100ZsoSWR and N100ZloSWR (bottom).

the external medium as well as matter driven outwards by the shock as it attempts to regain pressure equilibrium with its surroundings. As the star evolves, its ionizing luminosity decreases as the star expands and its surface temperature drops. In the solar metallicity case, this causes the ionization fraction of the photoionized gas (i.e. the fraction of atoms that have been photoionized) to drop as rate of recombination events rises above the rate of photoionization events. As a result, the temperature of the photoionized gas drops. For the runs at 0.1 Z$_\odot$, the luminosity in ionizing photons is much higher. As a result, the ionized gas remains at roughly 10^4 K. In addition, the radius of the ionization front is larger by around 50 per cent. The density of the ionized gas, however, remains the same, since the rate of expansion of the shell is limited by the sound speed in the ionized gas, which is approximately 10 km s^{-1} at 10^4 K. The larger radius can be attributed instead to a larger initial Strömgren sphere, as discussed in Section 3.2.

Inside the ionization front is a wind-driven bubble of radius $r_{\rm w}$. A free-streaming wind surrounds the star, as matter at the surface temperature of the star flows outwards. This material eventually shocks against the CSM, heating the gas to 10^6–10^7 K. Since the energy in the wind is much lower than the energy in ionizing photons, the pressure difference created by the wind is lower than that created by the ionizing photons, and as such $r_{\rm w}$ typically lags behind $r_{\rm i}$. There is a weak overdensity around the wind bubble, but most of this matter is photoheated and swept up by the photoionized bubble. In the runs at 0.1 Z$_\odot$, the wind is weaker still due to the

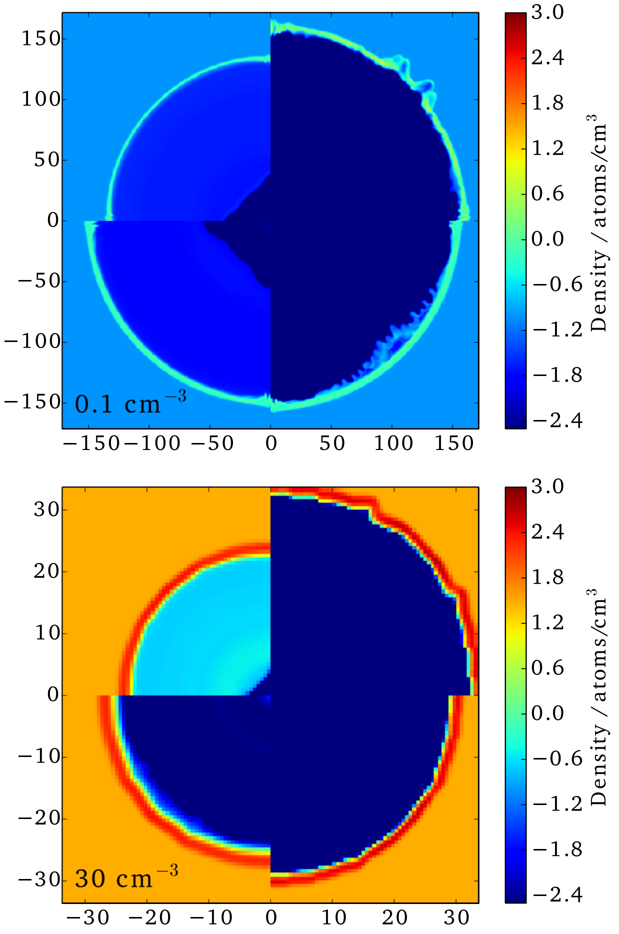

Figure 5. Slices in density through the simulation volume in the plane of the star and oriented along the grid z-axis for runs N0.1ZsoSWR (top) and N30ZsoSWR (bottom). The quadrants show the simulation at times, arranged counterclockwise from top left, 10 Myr, $t_{\rm SN}$, 1 Myr after $t_{\rm SN}$ and 2 Myr after $t_{\rm SN}$ (as in Fig. 3), where $t_{\rm SN}$ is 13.1 Myr. The image axes are in parsecs.

star's reduced opacity, meaning fewer particles are expelled from the surface of the star. Similar structures to those in the $Z_\odot$ runs are seen in these simulations, with comparable temperatures inside the wind bubble but with less mass redistributed by the wind. At 0.1 $Z_\odot$, the free-streaming wind phase is barely apparent. For the densest cases (Fig. 4), the wind bubble catches up to the ionization front. The consequence of this is that the outer edge of the bubble is heated to 10^6 K, whereas the unshocked wind inside the bubble is heated to 10^4 K by photons, leading to what might appear to be a smaller H II region embedded within a wind bubble. The interaction between the H II region and the wind is discussed further in Section 3.3.

Although the simulation is performed in a uniform medium, instabilities develop on the surface of the wind bubble. These can be observed in Fig. 5. The greatest deviations from spherical symmetry are aligned with the grid. In the absence of external turbulence, the most significant seed for instabilities is the grid structure itself. Ntormousi et al. (2011) note that along the grid axes, the cells are spaced closer together than cells along a diagonal. This means that the fluid is better resolved for surfaces normal to the grid axes. In these directions, the shell can be more easily compressed and is more susceptible to instabilities such as those described by (Vishniac 1983). This is an issue for our simulations, in which the winds are weak and the flows are marginally more efficient along the grid axes, where there is a higher effective resolution. Ntormousi et al. (2011) note that increased resolution does not help reduce the grid-aligned instabilities as the grid-aligned and grid-diagonal issue remains, and that the length-scales required to achieve convergence cannot be reached with the available computational resources. This is because thermal instabilities are governed by the Field length (Koyama & Inutsuka 2004), which at the dense shell is much smaller than the maximum spatial resolution achievable by contemporary 3D simulations of stellar feedback. Despite these issues, our results have converged with spatial resolution, as stated in Section 2.2.

Prior to the supernova, the ionization front is largely spherical, though some fluctuations can be observed in the shell (again, largely in the direction of the grid axes). Once the supernova occurs, the shock passes through the existing structures, gaining structure from the asphericity of the wind bubble, and causing fluctuations in the shell of the ionization front (which is now the shell of the supernova remnant). This effect is most apparent in the N0.1ZsoSWR image. In the N30ZsoSWR run, the wind has already reached the shell of the ionization front. We discuss in more detail in Section 3.3.

3.2 Evolution of the ionization front

The expansion of the ionization front is characterized by two phases. The first occurs of the order of the recombination time, $t_{\rm rec}$, where the ionization front approaches the Strömgren radius $r_{\rm st}$.[2] This is the radius inside which the rate of recombination events between free electrons and ions is equal to the flux of ionizing photons, and is given by

$$r_{\rm st} = \left(\frac{3}{4\pi} \frac{S_*}{n_{\rm i} n_{\rm e} \alpha_{\rm B}} \right)^{1/3}, \tag{1}$$

where S_* is the flux of ionizing photons from the star in photons per unit time, $\alpha_{\rm B}$ is the total recombination rate, and $n_{\rm i}$ and $n_{\rm e}$ are the ion and electron number density, respectively. $n_{\rm e} = n_{\rm i}$ if the ionization fraction $x = 1$, and hence for a fully ionized medium, $r_{\rm st}^3 \propto n_{\rm i}^{-2}$, which is an important result that will be referred to later in the paper. Note that this requires either a pure hydrogen CSM or one in which helium is only singly ionized. Indeed, we find in our results that the He III fraction is negligible. $r_{\rm i}$ reaches $r_{\rm st}$, assuming no hydrodynamic response from the gas, according to

$$r_{\rm i}(t) = r_{\rm st} \left(1 - {\rm e}^{-n_{\rm i} \alpha_{\rm B} t}\right). \tag{2}$$

The second phase is the hydrodynamic response of the gas due to thermalization to 10^4 K by photoionization. This phase is described analytically by Spitzer (1978):

$$r_{\rm i} = r_{\rm st} \left(1 + \frac{7}{4} \frac{C_{\rm i} t}{r_{\rm st}}\right)^{4/7}, \tag{3}$$

where $C_{\rm i}$ is the speed of sound in the ionized gas ($\simeq 10\,{\rm km\,s^{-1}}$). In this phase, the photoionized gas is heated to approximately 10^4 K, which creates a pressure gradient at the ionization front. This causes the density inside the ionized gas to drop and the remaining mass to be deposited around the ionization front as a dense shell. The recombination time is inversely proportional to the density of the medium: 1.2 Myr for 0.1 atoms cm^{-3} and 4 kyr for 30 atoms cm^{-3}. Thus, for dense media, the ionization front reaches $r_{\rm st}$ on a time-scale much shorter than the lifetime of the star. By contrast, the photons

---

[2] Note that this is distinct from the radius of the supernova remnant, which we label $r_{\rm s}$.

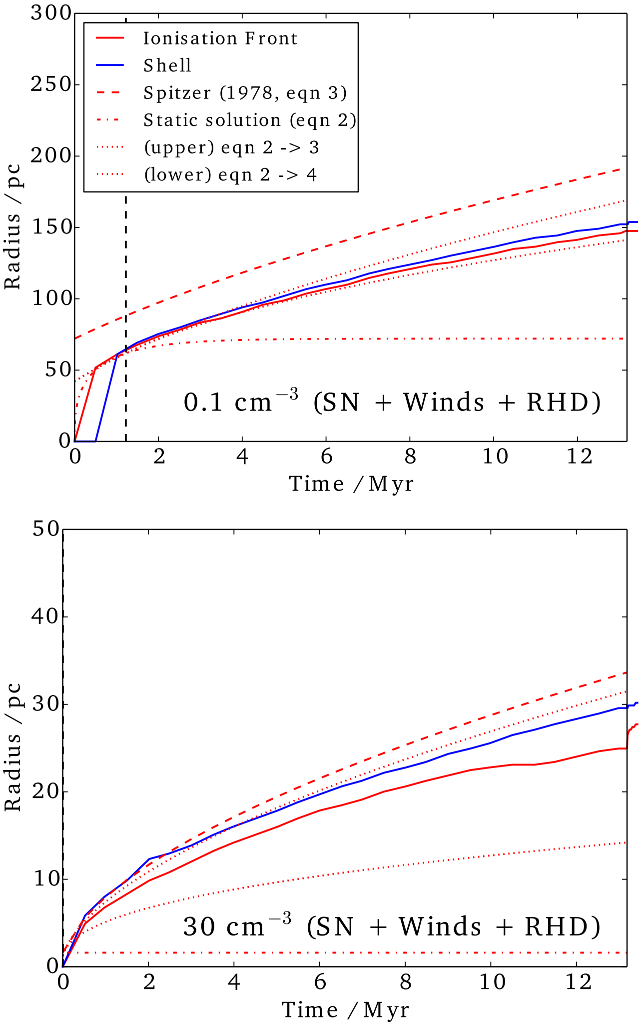

Figure 6. Radius of the ionization front against time up to $t_{\rm SN}$. The upper figure shows data for the N0.1ZsoSWR run, while the lower figure shows the N30ZsoSWR run data. The solid blue line is the extent of the dense shell (the maximum radius at which $n_{\rm H} > n_{\rm H,ini}$), while the solid red line is the maximum radius at which more than 10 per cent of hydrogen atoms are ionized. A vertical dashed line is plotted at the recombination time at the given density, $t_{\rm rec}$. The upper dashed curve is the Spitzer (1978) given by equation 3. The upper dotted curve is the same equation, but solved starting from time $t_{\rm rec}$ using the radius equation 2 at $t_{\rm rec}$. The bottom curve uses the same method but uses equation 4 instead. This equation assumes that the falling UV photon flux leads to the supply of ionized gas being held constant. The dot–dashed curve shows the hydrostatic evolution to the Strömgren radius $r_{\rm st}$ given in equation 2.

in more diffuse media take around 10 per cent of the lifetime of the star to reach $r_{\rm st}$. This has consequences for the evolution of the front. In Fig. 6, the ionization front of the star in run N30ZsoSWR reaches the Strömgren radius almost immediately, and then follows the Spitzer solution until the flux of ionizing photons drops and the ionization front expands less rapidly. By contrast, the ionization front in run N0.1ZsoSWR does not reach $r_{\rm st}$ before it begins to respond hydrodynamically. However, the solutions are only weakly coupled: since the Strömgren radius is 70 pc at 0.1 atoms cm^{-3} and 1.6 pc at 30 atoms cm^{-3}, and the speed of sound for both densities inside the ionization front is around 10 km s^{-1} $\simeq$10 pcMyr^{-1}, a sound wave would take five times as long to cross $r_{\rm st}$ as the recombination time at 0.1 atoms cm^{-3} (37 times at 30 atoms cm^{-3}).

We thus introduce a solution in which the ionization front expands to $r_{\rm st}$, and then is allowed to expand according to equation 3. This solution is valid until the photon flux begins to fall significantly, and the ionization fraction falls below 1. At this point equation 1 is no longer applicable, since the number of recombinations per second exceeds the flux of photons. In one scenario, the photons can no longer ionize new gas, and the mass of the bubble is constant, i.e. $r_{\rm i}^3 n_{\rm i}$ = constant. Solving the jump conditions given in Spitzer (1978) as used to derive equation 3, but with $r_{\rm i}^3 \propto n_{\rm i}^{-1}$ instead of $n_{\rm i}^{-2}$, we find

$$r_{\rm i} = r_0 \left(1 + \frac{5}{2}\frac{C_{\rm i}(t - t_{\rm rec})}{r_0}\right)^{2/5}, \tag{4}$$

where r_0 is the radius at $t_{\rm rec}$ ($\leq r_{\rm st}$). We also plot this in Fig. 6. Run N0.1ZsoSWR follows the Spitzer solution closely before falling between it and equation 4 after 4 Myr. While the gas is no longer being ionized up to $r_{\rm st}$ as in the Spitzer solution, there is some residual photoionization that keeps the gas partially photoionized.

The momentum and kinetic energy of the shell can be approximated with reasonable accuracy by using these radial solutions, and assuming that all the shell mass is concentrated at $r_{\rm i}$, travelling at d$r_{\rm i}$/dt. The mass of the shell can be calculated by subtracting the ionized bubble mass, calculated using $r_{\rm s} \propto n^{-2/3}$ as above, although the transition between fully-ionized and partially-ionized regimes as the star's ionizing luminosity drops complicates finding an exact analytic solution. This solution agrees roughly with the energy and momentum of the shell given in Walch et al. (2012). Despite the large quantity of energy in ionizing photons leaving the star throughout its lifetime, only 0.1–0.01 per cent of this energy is transferred to kinetic energy in the shell, most of it being lost as radiation. The key impact that photoionization has in terms of feedback from the star is to alter the density of the gas around the star prior to supernova. We return to this subject in Section 4.

In our simulations, we also include helium ionization, which is provided by default in RAMSES-RT. Typically, photoheating from hydrogen is the dominant process, and we do not notice much difference if we remove helium. Even before the temperature of the star has dropped noticeably, the helium inside the ionization front is not completely ionized to He II, and very little is ionized to He III. Many photons at energies that ionize helium to He III are able to escape the ionization front entirely. A small amount of leakage, i.e. photons escaping the shell at $r_{\rm i}$, is also observed in hydrogen-ionizing photons in the runs at 0.1 atoms cm^{-3}. Since the gas began responding hydrodynamically at this density before the ionization front had reached $r_{\rm st}$, the ionization front lags behind $r_{\rm st}$. As a result, a number of photons reach the shell and some are able to pass through it without being absorbed. Subsequently, the value of r_0, given by $r_{\rm i}(t_{\rm rec})$, that we use in equation 4 is lower than $r_{\rm st}$ for the run at 0.1 atoms cm^{-3}. Additionally, the hot, shocked gas inside the wind bubble thermally ionizes the CSM up to $r_{\rm w}$. This allows the photons to pass up to $r_{\rm w}$ without being absorbed by neutral hydrogen.

We should note that the external medium in our simulations is static and largely unpressurized. Raga et al. (2012) introduce a term to Spitzer's equation to account for thermal and turbulent pressure in the CSM, and determine that there is a point at which the pressure inside the ionization front is equal to that outside, and the front cannot expand further. Tremblin et al. (2014) expand on this by simulating ionization fronts with external turbulence. They find that while the solutions are constrained by external pressure, existing momentum in the shell can cause the simulated shells to overshoot Raga et al. (2012)'s analytic solution.

One further consideration is that metal cooling and heating rates in photoionized gas are typically different from those in neutral gas. Draine (2011) states that the equilibrium temperature in the gas may vary from 5000 to 15 000 K, depending on its metallicity, density and the photon flux. In this work, we do not include these rates, though in practice they may become important for modelling H II regions accurately.

3.3 Expansion of the wind bubble

The wind luminosity of our model star is significantly lower than the luminosity in ionizing photons. None the less, the effect of the wind is visible in the temperature and density profile, as described in 3.1. In Fig. 1, the wind luminosity is roughly constant until 10 Myr, when the mass-loss rates increase significantly before the star explodes as a supernova at 13.1 Myr in the solar metallicity runs. In Fig. 7, we plot the radial expansion of the stellar wind bubble for runs at 0.1 and 30 atoms cm^{-3}, both in the presence and in the absence of an ionization front. In the case without photoionization, the wind expands initially according to the adiabatic solution of Avedisova (1972) and Castor et al. (1975).

Once the structure loses a substantial portion of its energy to radiative cooling, the shell begins to decelerate. Curiously, after a few Myr in both runs N0.1ZsoSW and N30ZsoSW, the shells appear to reach a state where it either decelerates very slowly or not at all. From equation 54 of Weaver et al. (1977), if the shell's acceleration is negligible, we obtain a speed of the shell around the wind bubble $V_{\rm shell}^2 = P/\rho_0$, where P is the pressure driving the shell and ρ_0 is the mass density in the external medium. At 5 Myr, we find that $V_{\rm shell}$ is 2.55 km s^{-1} in N0.1ZsoSW and 0.33 km s^{-1} in N30ZsoSW, though in the latter case $V_{\rm shell}$ drops below this value at later times. These profiles are overplotted on Fig. 7. For $V_{\rm shell}$ to be constant, the pressure at the shell also needs to be constant. In run N0.1ZsoSW, the pressure drops throughout the main sequence of the star but is maintained at a stable value once the wind luminosity increases at late times. In run N30ZsoSW, a similar effect occurs, although the effect is more dramatic, as the pressure inside the bubble falls by then rises by an order of magnitude once the wind luminosity

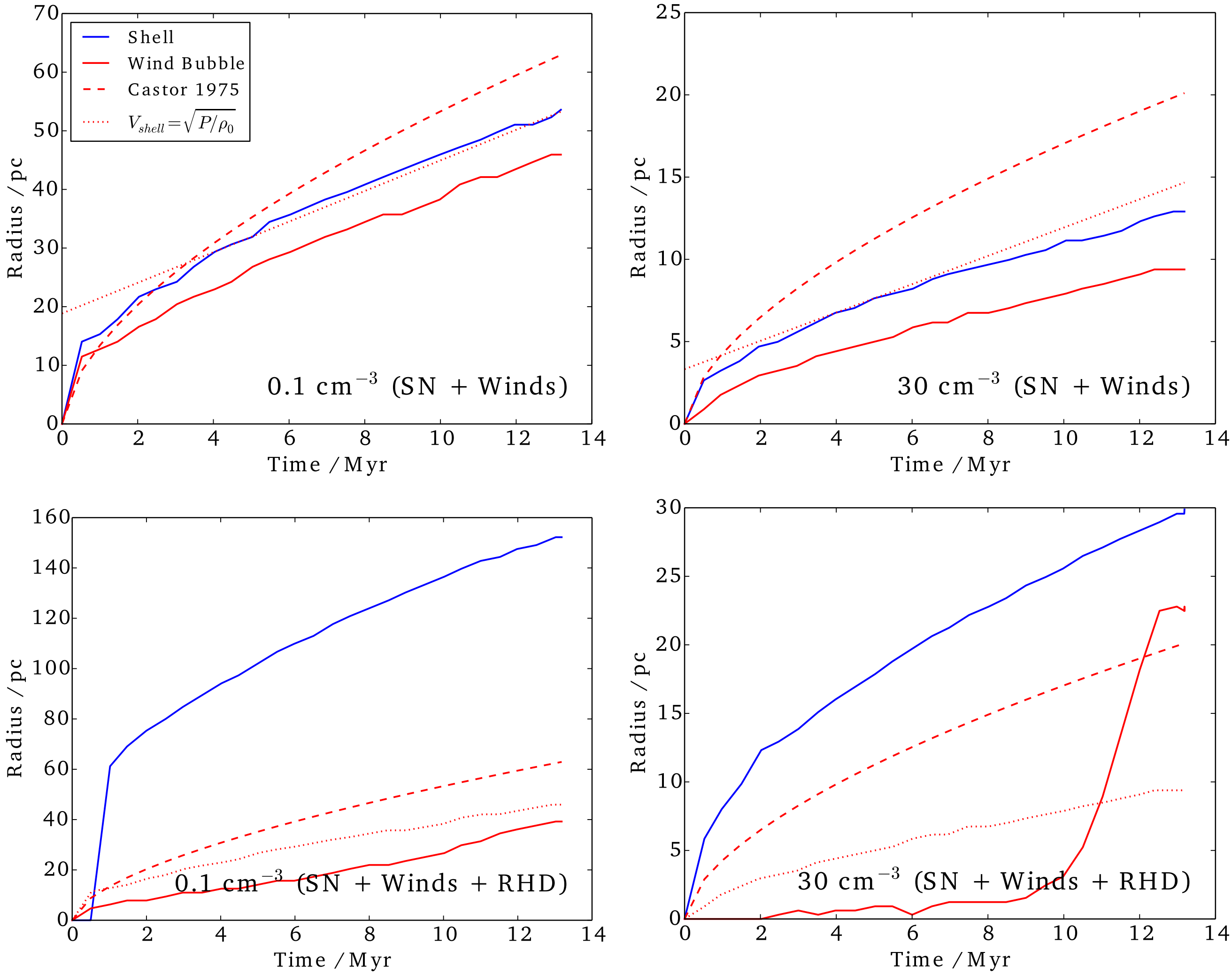

Figure 7. Radii of wind bubbles against time in N0.1ZsoSW (top left), N30ZsoSW (top right), N0.1ZsoSWR (bottom left), N30ZsoSWR (bottom right). The radius of the shell (the maximum radius r at which $n(r) > n_0$ for a background density of n_0) is plotted as a solid line. In simulations including photoionization, the shell radius lies at $r_{\rm i}$, whereas in simulations without photoionization it is found at $r_{\rm w}$). The radius of the hot bubble (a heuristic value determined as the maximum radius at which $T > 2 \times 10^3$ K in runs without photoionization, and 2×10^4 K with photoionization) is plotted as a red line. The adiabatic solution for a wind bubble given by Avedisova (1972), Castor et al. (1975) is plotted as a red dashed line. In the top figures, the solution for which the internal pressure force of the bubble balances the deceleration from matter accretion by the shell is plotted as a red dotted line, positioned vertically to intersect the shell radius at 5 Myr. In the bottom figures, the hot bubble in the simulations containing only wind (the solid red line in the top figures) is plotted as a red dotted line.

increases. By the end of the lifetime of the star, the pressure inside the shell at $r_{\rm w}$ in run N30ZsoSW is far higher than the pressure at the inner edge of the wind bubble. This is because although the temperature of the shell is only around 20 K, the density of the shell is far higher than that inside the wind bubble. At this density and temperature, we would have to consider cooling from molecules in order to properly determine the gas pressure. The radial expansion of the bubble is influenced to some extent by instabilities in the shell, which cause differences in the radial expansion of the shell across its surface, though from visual inspection these differences are small.

When we include the ionization front, the wind bubble radius in N0.1ZsoSWR expands more slowly than in the same run without photoionization. A more dramatic effect is seen in run N30ZsoSWR, where the wind bubble is prevented from expanding beyond 1 pc until the star reaches an age of 10 Myr. This bubble is undersampled in our plots due to the small number of cells inside 1 pc, leading to the bubble being identified as having zero radius for some timesteps. In addition, it is only fractionally hotter than the photoionized gas, making detection difficult. After 10 Myr, the wind bubble rapidly expands to the inner edge of the shell of the ionization front, far beyond its extent in the simulation without photoionization. This is because the pressure inside the ionized gas is higher than the external medium, and so the expansion of the wind is resisted, as per Weaver et al. (1977). The pressure $P_{\rm i}$ inside the ionization front can be approximated as $2n_{\rm i}k_{\rm B}T$, where $n_{\rm i}$ is the number density of the ions and $T = 10^4$ K, and the factor of 2 accounts for electrons (slightly higher if we include twice-ionized helium). Using equation (1) for a constant photon flux and ionization fraction, $P_{\rm i}$ scales as $r_{\rm i}^{-3/2}T$ as long as the gas remains in ionization equilibrium. In our simulations, the pressure drops faster due to the decreasing photon flux throughout our simulation. This effect is particularly noticeable at around 10 Myr, the same time that the wind luminosity increases. As a result, the wind bubble radius grows much faster after 10 Myr.

There are a few reasons why this effect is more pronounced in the denser medium. First, the final value of $r_{\rm i}$ for N0.1ZsoSWR is less than 2 Strömgren radii, compared to a factor of several for N30ZsoSWR (see Fig. 6). As a result the pressure drops faster in the denser run from the initial value since as stated above, $P_{\rm i} \propto r_{\rm i}^{-3/2}T$. Secondly, the initial pressure inside the ionized gas is much lower in N0.1ZsoSWR than N30ZsoSWR as the initial density is 300 times lower. This means that the wind in the diffuse case is never completely prevented from expanding. Thirdly, once the photoionized gas begins to recombine as the photon flux drops, the effect of collisional cooling in the denser gas is stronger than in the more diffuse gas.

Hence for winds expanding inside ionization fronts in diffuse media, which have a low initial pressure but a less marked change in pressure over time, the wind expands more slowly than in a neutral medium, but not much more. By comparison, in dense environments, the ionized gas has a high initial pressure that rapidly drops as $r_{\rm i}$ expands. In this case, the wind bubble cannot expand until the front grows and the ionization fraction drops leading to a lower temperature, at which point the wind bubble expands rapidly.

4 THE PROPERTIES OF THE SUPERNOVA REMNANT

4.1 Role of pre-supernova stellar evolution

At $t_{\rm SN}$, the star explodes, creating a supernova remnant that expands into the surrounding medium. $t_{\rm SN}$ is 13.2 Myr for the star at $Z_{\odot}$ and 15.8 Myr for 0.1 $Z_{\odot}$. The radial expansion of the supernova remnant depends on the structure of the CSM prior to the supernova. Figs 8 and 9 show the radial evolution of the supernova remnant for the runs at 0.1 and 30 atoms cm^{-3} at solar metallicity for simulations including just a supernova, a supernova plus photoionization, and a supernova plus winds and photoionization (for the sake of brevity, we omit simulations with winds but without photoionization). The cases in which a supernova explodes into a uniform medium without stellar winds or photoionization are well-studied in the literature. The Sedov solution (Sedov 1946) describes a fully-adiabatic remnant, which our results quickly deviate from as the supernova bubble loses thermal pressure to radiative cooling. A better comparison is made when we overplot an empirical formula for the radial expansion of a supernova remnant derived by Cioffi et al. (1988), who include radiative cooling in their models. Our results lie slightly under their curve in the run N0.1ZsoS, but the difference is not marked. In n30zsos, the agreement with Cioffi et al. (1988)'s formula is much better. In both cases, the shell begins to spread, i.e. the difference between the inner and outer radius of the shell grows. This is because as the bubble cools, it loses pressure, to the point where the thermal pressure in the shell is higher than that inside or outside the shell radius. In N30ZsoS, the gas cools so rapidly that towards the end of the simulation most of the bubble falls below our threshold of 2×10^3 K. Once the pressure in the bubble falls below the pressure in the shell, the remnant becomes momentum-conserving, and decelerates as its kinetic energy is transferred to matter accreted by the shell from the external medium.

When we include photoionization prior to the supernova, a large underdensity is created inside the ionization front, and the displaced matter is piled into a shell at $r_{\rm i}$. During the adiabatic phase of expansion, the shock radius follows the Sedov solution, i.e. $r_{\rm s}(t) \propto n^{-1/5}t^{2/5}$. Hence for lower density environments, the supernova remnant can expand more rapidly. Typically, the pressure inside the supernova bubble is much greater than that inside the H II region or wind bubble. Further, as the density is lower, the energy loss rate from radiative cooling is lower. The effect of photoionization from the star is thus to cause the remnant to expand more rapidly and lose less energy to radiation.

The supernova blastwave reaches the ionization front within 1 Myr in both N0.1ZsoSR and N30ZsoSR. At this point, the velocity of the shell drops considerably as the shock transfers its momentum to the shell. The final radius of the supernova is increased by the presence of an ionization front. In fact, since in both cases the final radius of the ionization front is greater than the radius of the supernova remnant in N0.1ZsoS and N30ZsoS after 7 Myr, the radial extent of the supernova remnant appears to be largely governed by the pre-supernova photoionization. Adding stellar winds does not appear to significantly change the radial evolution of the remnant. The diffuse medium exhibits some radial variations from features on the surface of the shell transmitted from the wind bubble's structure by the supernova shock (see Fig. 5), but the overall radial evolution is similar. This lack of influence is due to the significantly lower energy in the wind compared to the ionizing photons and supernova blast.

In Fig. 10, we plot the evolution of the kinetic and thermal energy in each of the runs at 0.1 and 30 atoms cm^{-3}, adding physical processes in turn to quantify their influence on the energetics of the supernova remnant. The result of the cooling H II region due to decreasing ionizing photon flux is most clearly seen in the runs at 30 atoms cm^{-3}. This is because the higher density leads to more efficient cooling than in the 0.1 atoms cm^{-3} medium. By contrast, the thermal energy from the wind bubble grows at the same time,

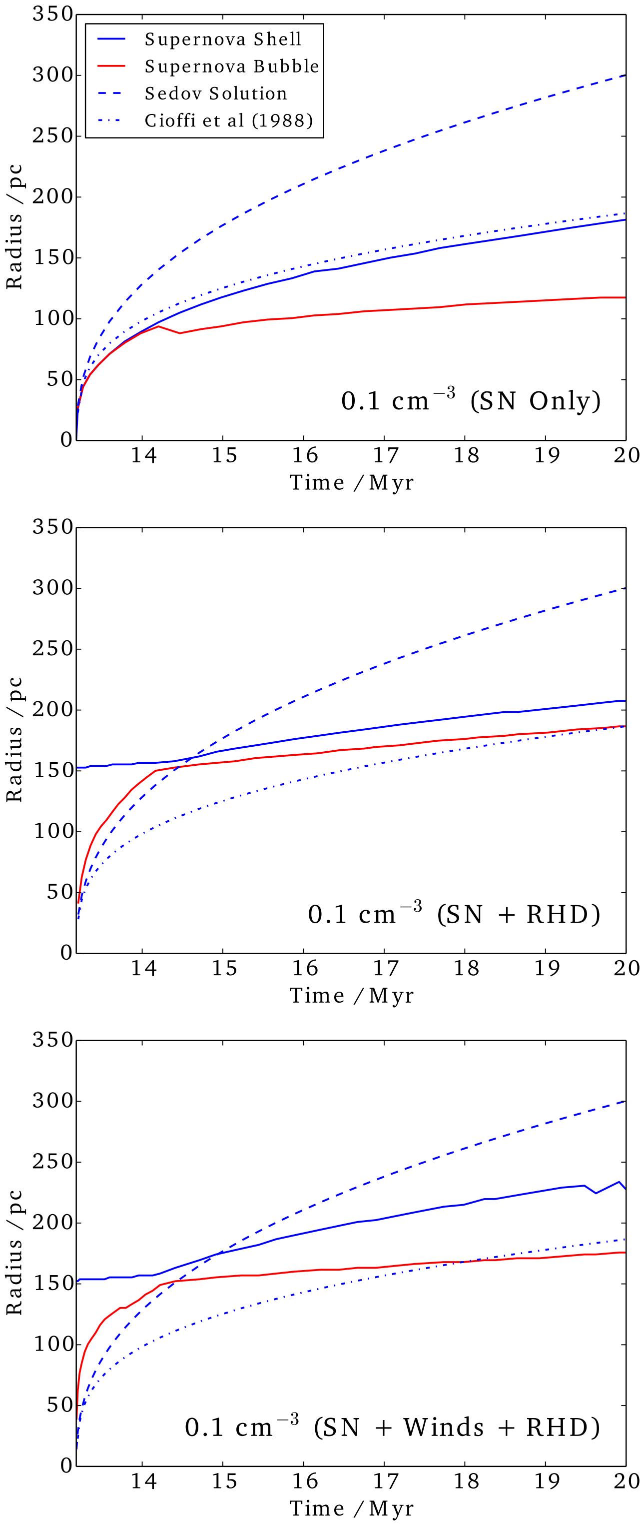

Figure 8. The radial evolution of the supernova remnant with time. The top figure shows N0.1ZsoS, the middle shows N0.1ZsoSR and the bottom shows N0.1ZsoSWR. The radius of the shell $r_s(t)$ (the maximum radius r at which $n(r) > n_0$ for a background density of n_0) is plotted as a solid blue line. The radius of the hot bubble (the maximum radius at which $T > 2 \times 10^3$ K) is plotted as a solid red line. The Sedov solution for the given medium is plotted as a blue dashed line, while the solution found in Cioffi et al. (1988) is plotted as a blue dot–dashed line.

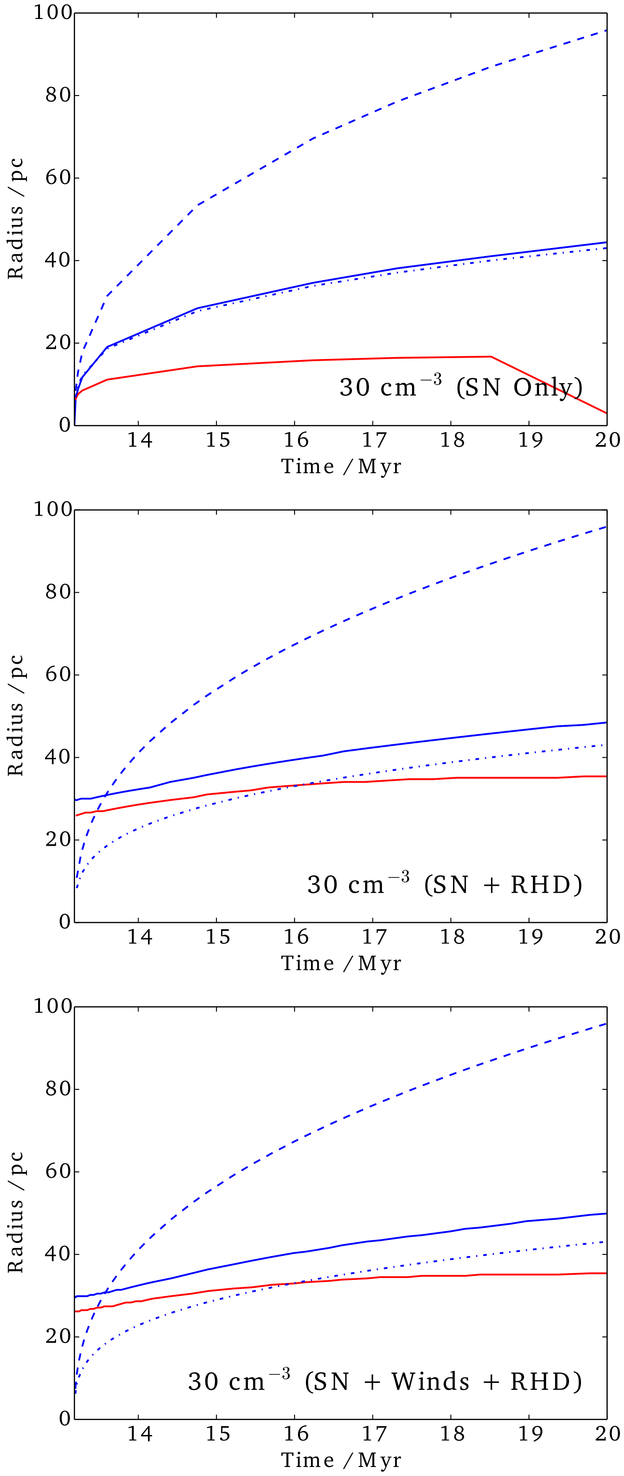

Figure 9. As for Fig. 8, but for N30ZsoS (top), N30ZsoSR (middle) and N30ZsoSWR (bottom).

due to a higher wind luminosity from the star, though at two orders of magnitude lower energies than that deposited by photoionization. Once the supernova occurs, 1.2×10^{51} erg are deposited around the star as thermal energy. This quickly reaches an equipartition with kinetic energy, which sets up reverse shocks inside the r_s. In runs N0.1ZsoS and N30ZsoS, the solution quickly arrives at a thermal

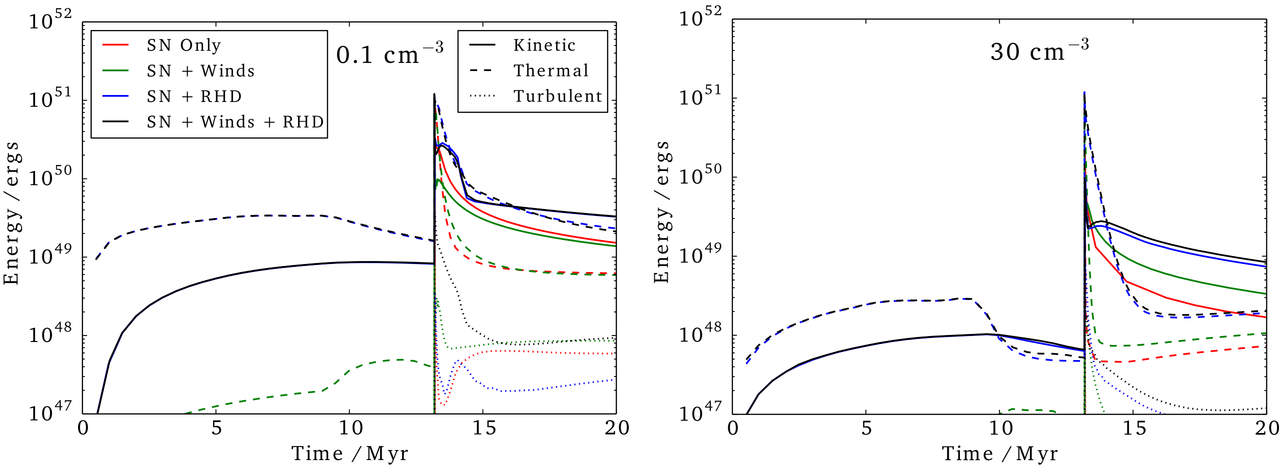

Figure 10. Energy in the CSM over time with different physics included at solar metallicity. The left-hand plot shows the energy in runs at 0.1 atoms cm^{-3}. Red lines are for the run implementing only the supernova at $t_{\rm SN}$ (labelled 'S'). Green lines are for runs including a supernova and stellar winds but no radiation ('SW'). Blue lines are for runs including a supernova and radiation but no winds ('SR'). Black lines are for runs implementing all three processes ('SWR'). The solid lines are kinetic energy, the dashed lines are thermal energy and the dotted lines are turbulent energy, which is measured as the kinetic energy of all non-radial velocity components. The right-hand plot is the same, but for the runs at 30 atoms cm^{-3}.

equilibrium, with kinetic energy dropping due to accretion of stationary matter outside $r_{\rm s}$. In N30ZsoS, the thermal energy rises after a time, an effect reported by Thornton et al. (1998), who attribute this to accretion of thermal energy from the external medium. We find that the external medium does indeed have sufficient thermal energy to do this, although the temperature is of the order of 10 K, and so it is not clear that radiative cooling is properly captured by our cooling function at these temperatures. Adding a stellar wind to the runs at 0.1 atoms cm^{-3} does not change the results significantly, since the energy contribution from winds is insignificant. By comparison, winds have a significant impact on the energetics of the supernova remnant at 30 atoms cm^{-3}, since the early cooling rate of the supernova is reduced owing to the pre-evolved underdensity inside the wind bubble. Once radiation is added, the kinetic energy in the 0.1 atoms cm^{-3} runs plateaus while the shock travels through the ionized gas, then drops as the shock interacts with the shell at $r_{\rm i}$. The effect of stellar winds on the kinetic energy is small in the runs at 0.1 atoms cm^{-3}, with a small decrease in kinetic energy due to the shock interacting with the wind bubble. By contrast, the runs at 30 atoms cm^{-3} gain energy when winds (but not photons) are included because the denser medium makes the initial shock more susceptible to cooling than the diffuse medium.

Chevalier (1977) state that only a few per cent of the energy injected into the ISM by supernovae is transmitted to the gas around it, with the rest lost to radiative cooling. We find that after 2 Myr, N0.1ZsoS has 3 per cent of the initial 1.2 × 10^{51} erg in kinetic energy (see Table A1), while N30ZsoS only retains 0.4 per cent. Including photoionization and winds has a small impact on this value at 0.1 atoms cm^{-3}, but N30ZsoSWR is able to retain 1.5 per cent of its energy, roughly four times as much as without photoionization, due to less efficient cooling in the low-density gas inside $r_{\rm i}$.

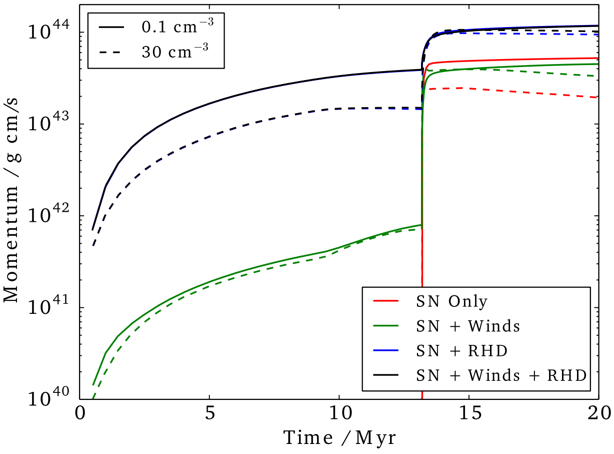

Figure 11. Total momentum over time with varying physics included. All runs are shown at $Z_\odot$. The solid lines show the runs at 0.1 atoms cm^{-3}, while dashed lines show the runs at 30 atoms cm^{-3}. Colours are as stated in the legend and in Fig. 10.

Our N0.1ZsoS run energy values are in good agreement with Thornton et al. (1998), whereas we find generally lower energies for the run N30ZsoS by a factor of a few (see Table A2 for values). Our simulations include more efficient cooling to lower temperatures, since Thornton et al. (1998) do not treat cooling below 1500 K. Similarly, Cioffi et al. (1988) do not consider cooling below 10^4 K, whereas, as Chevalier (1974) notes, much of the energy in the shell will be lost as it cools to around 10 K. Another aspect of their work is that they introduce the largest portion of their initial supernova energy as kinetic energy (as do Cioffi et al. 1988), whereas our supernova is purely thermal (as in Chevalier 1974). It is possible that the early evolution of the shock may differ as a result, despite the fact that our simulations are adequately resolved to capture the initial cooling of the thermal blast. Cioffi et al. (1988) give a description of this early phase in the presence of a mostly-kinetic shock. Durier & Dalla Vecchia (2012) find that the initial partition of energy in a blastwave should not affect the final result, though they do not as yet include radiative cooling in their work.

When we look at the momentum of the gas in Fig. 11, the time evolution is somewhat simpler. It is interesting that the momentum from the stellar wind appears to be only weakly correlated with density. From Weaver et al. (1977), we can estimate the wind shell momentum as being proportional to $\rho_0^{1/5}$, assuming all the matter inside $r_{\rm w}$ is displaced to $r_{\rm w}$, and that the shell velocity is $\dot{r}_{\rm w}$. This weak density dependence is offset by more efficient cooling in denser runs, which is not considered in Weaver et al. (1977). Performing a similar analysis using the Spitzer solution (equation 3) for the ionization front, we find that the momentum $p_{\mathrm{i}} = \rho_0 r_{\mathrm{s}} C_{\mathrm{i}} (1 + 7/4 C_{\mathrm{i}}/r_{\mathrm{s}} t)^{9/7}$. Since $r_{\mathrm{s}} \propto \rho_0^{-2/3}$, we find that the momentum is proportional to $1/\rho_0$ (assuming that the power of $9/7 \simeq 1$, and noting that C_{i} is constant with density as the ionized gas is at 10^4 K in both cases). If we assume the limit during the late evolution in which $r_{\mathrm{s}} \propto n^{-1/3}$, the momentum is constant with respect to ρ_0. Hence, the momentum in the runs at 30 atoms cm^{-3} is lower than the run at 0.1 atoms cm^{-3}, though not 300 times lower, since the runs at 0.1 atoms cm^{-3} fall below the Spitzer solution (see Fig. 6).

Once the supernova occurs and the shock reaches the edge of the H II region, there is no visible impact from the supernova shock and the shell around the H II region merging on the momentum. The final momentum in N0.1ZSOSR is only around 10 per cent higher than the sum of the momentum in N0.1ZSOSR before the supernova and the final momentum of N0.1ZSOS, suggesting that the supernova blastwave's momentum is mostly unchanged by the H II region, and the main contribution from photoionization is additional momentum from the shell around the photoheated gas. By contrast, the final momentum in N30ZSOSR is much higher than the sum of the pre-supernova momentum in N30ZSOSR and the final momentum in N30ZSOS. This is a result of the effect discussed above, where in denser environments, the H II region lowering the density of the CSM prior to the supernova prevents the remnant from losing a significant portion of its energy before it becomes momentum-driven. As with the results for the kinetic energy, winds have a limited impact on the momentum when photoionization is included. The inclusion of wind but not photoionization reduces the final momentum in N0.1ZSOSW but raises it N30ZSOSW. Interestingly, the momentum after the supernova in runs N0.1ZSOSW and N30ZSOSW converges to the same value, 4×10^{43} g cm s^{-1}, suggesting that the wind has a similar effect to the H II region in determining the momentum evolution of the supernova independently of the external medium.

In the runs at 30 atoms cm^{-3} some 2–3 Myr after the supernova has exploded, the remnant appears to lose momentum, rather than conserving it. This is because as the shell cools, its pressure tends towards that of the external medium, causing the force resisting the expansion of the supernova remnant to become non-negligible. In the presence of an external heating term (not included in this study), we would expect this effect to be visible in the run at 0.1 atoms cm^{-3} as well. A final curious effect is that the post-supernova momentum is roughly constant with respect to ρ_0 in runs with winds or radiation but not without. We attribute this to the fact that, again, the underdensity swept out by these processes limits the early cooling of the supernova shock and hence reduces the impact of density on radiative losses. That being said, the empirical fit of Cioffi et al. (1988) finds that the final momentum should be related to density by $\rho_0^{-1/7}$, i.e. the momentum deposited in their simulations is more or less independent of density even when not in the presence of winds or photoionization. When comparing our simulations to these authors, we find a final momentum that is a factor of 2–3 lower than their analytical formula in both N0.1ZSOS and N30ZSOS, though Cioffi et al. (1988) note that even their simulations reach only 80 per cent of the value derived from the formula, suggesting that the analytic expression diverges by a small amount from the simulated shock. One notable difference between our work and Cioffi et al. (1988) is that the latter allows cooling in the shell only down to 10^4 K. Another is that our shell begins to spread as the pressure inside the shell drops. Some momentum is also lost to turbulence, which we discuss below. Our values for momentum agree with the results of Walch & Naab (2014) to within the spread of values found by these authors. These authors do not include stellar winds or a varying photon flux but do include a structured (non-turbulent) medium around the star. This suggests that the key effect is the evacuation of the dense gas by the H II region, and that other aspects of the pre-supernova CSM evolution do not significantly alter the final momentum injected into the ISM.

In Fig. 12, we plot energies and momenta for all of the runs containing both winds and photoionization. In solar metallicity environments, these results evolve between the profiles already presented for runs N0.1ZSOSWR and N30ZSOSWR. At 0.1 $\mathrm{Z}_\odot$, the star survives longer and has a stronger photon flux. The rate at which the supernova remnant cools is also significantly reduced. Whereas for the runs at $\mathrm{Z}_\odot$, we find a final momentum of 10^{44} g cm s^{-1} mostly independent of density, at 0.1 $\mathrm{Z}_\odot$ we find roughly twice that value with some variation from this value as a function of density. The results suggest that the momentum from a supernova blast exploding inside a H II region is kept constant with respect to the external density by the reduced cooling inside the low-density photoheated bubble, and the small variation in the final value is dependent largely on the momentum from the shell around the ionization front, which is larger in the low-metallicity case owing to reduced cooling and increased UV flux from the star.

In contrast to the bulk kinetic energy, turbulence is introduced mainly by the stellar winds, which transfer their aspherical structures to the supernova, which develops non-radial flows in response. We adopt a simple, robust measure for the energy in turbulence as the energy in all non-radial velocity components in the simulation. We find that turbulent flows account for less than 1 per cent of the kinetic energy of the system before the supernova. Similarly, once the supernova remnant has cooled, only 1 per cent of the kinetic energy of the system after the supernova is found in turbulent flows, in agreement with Gull (1973). However, 10 per cent of the momentum is in non-radial velocity components. These results appear to be independent of metallicity.

5 CONCLUSIONS

We have described the results of a study in which a single 15 $\mathrm{M}_\odot$ star deposits mass, momentum and energy into its surroundings. Our simulations reproduce the quasi-spherical matter distribution around a star in various environments using the M1 method for radiative transfer, with physically-motivated models for stellar winds and ionizing photon fluxes and a supernova at the end of the lifetime of the star. As the star evolves, the flux of ionizing photons decreases as the stellar radius grows and the surface temperature drops. As a result, we find that for the more diffuse media the ionization front deviates from the Spitzer (1978) solution, and suggest an alternative model that takes into account the recombination time and decreasing ionization fraction inside the ionization front. As in previous work, the amount of energy in ionizing photons transferred to the ISM is of the order of 0.1–0.01 per cent, with most of it lost to radiative cooling from recombination processes.

The expansion of wind bubbles is highly sensitive to changes in the wind luminosity and ionizing photon flux throughout the stellar lifetime. Their evolution is determined by the pressure balance between the edge of the wind bubble and the inside of the H II region. This balance changes throughout the simulation as the H II region expands. While the wind luminosity grows in the final stages of stellar evolution, the photon flux drops and the H II bubble leaves ionization equilibrium. In the denser environments, this balance means that the wind bubble is even effectively prevented from forming until the horizontal giant branch (HGB) phase, at which

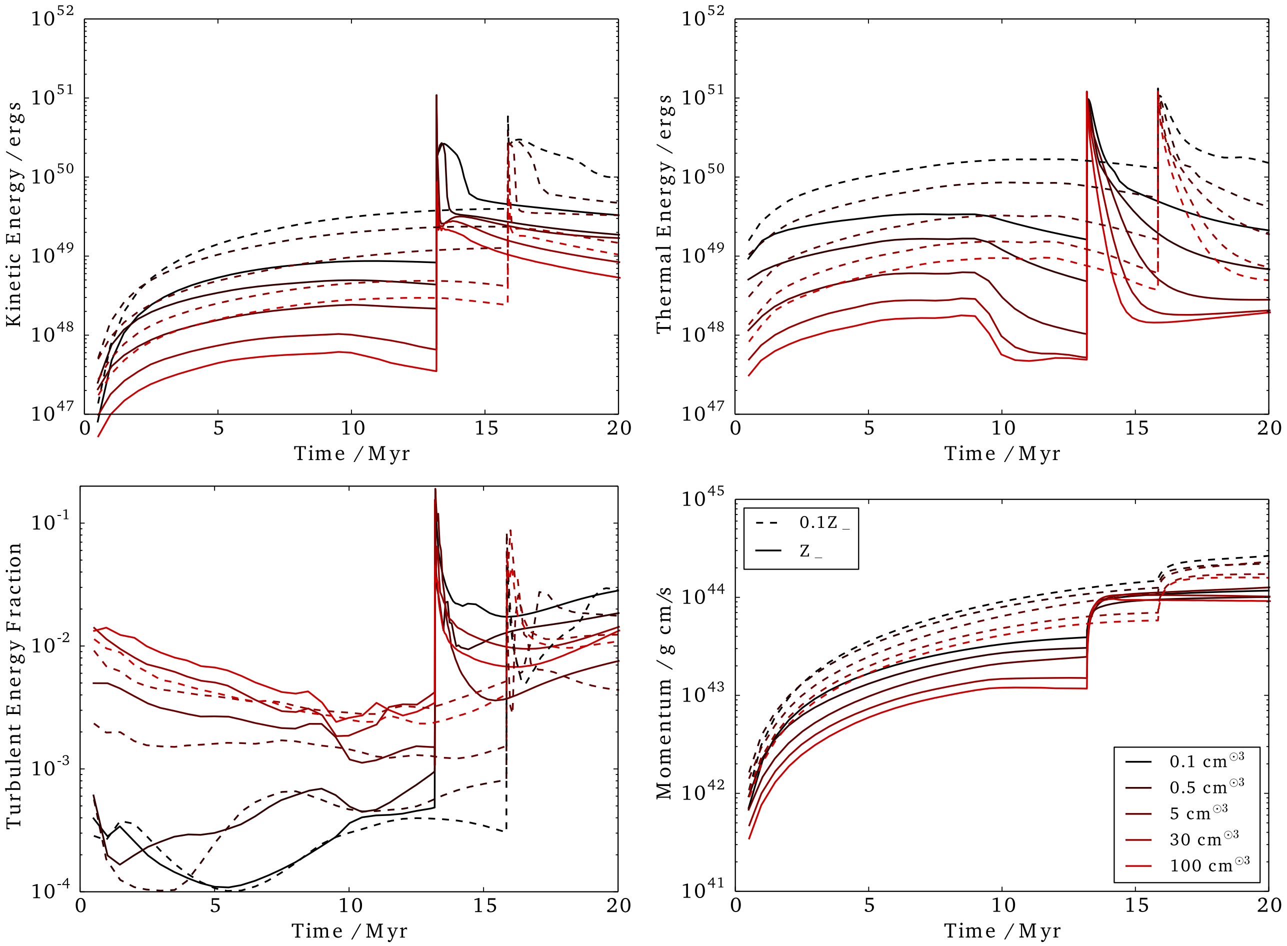

Figure 12. Evolution of the properties of the CSM over time for each of the runs containing winds and photoionization. Shown are kinetic energy (top left), thermal energy (top right), turbulent energy fraction (bottom left) and momentum (bottom right). The $Z_{\odot}$ runs are shown as a solid line and the 0.1 $Z_{\odot}$ runs as dashed lines. The turbulent energy fraction is determined by measuring the fraction of the kinetic energy found in non-radial velocity components.

point it expands rapidly out to the edge of the H II bubble. The photons from the star then heat the unshocked wind inside to 10^4 K, leading to a structure that appears to be a wind bubble with a smaller H II region embedded within it. If this effect occurs in more general cases, it could be an important consideration when modelling the temperature and structure of H II regions. Even in uniform environments, the structure of the CSM prior to the supernova is dependent on the interplay between the varying winds and UV flux and the initial gas density. We find that the winds from stars of the mass studied in this paper do not significantly contribute to the energy of the ISM, though we have not considered winds from more massive stars. Agertz et al. (2013) tabulate the energy from winds in a population of stars and find a much higher value, suggesting that Wolf–Rayet winds from more massive stars than the one modelled here may be more significant.

The supernova explodes inside an underdensity surrounded by a dense shell carved out by ionizing photons and winds from the supernova progenitor star. The ionization front both provides momentum to the ISM and reduces the loss of energy in the supernova shock from radiative cooling due to this underdensity. The former process is more important in diffuse media and the latter is more important in denser media. For solar metallicity environments, a final value of 10^{44} g cm s^{-1} is found for the momentum of the remnant, and 2×10^{44} g cm s^{-1} for 10 per cent solar metallicity environments, with more variation in the lower metallicity runs with different initial densities. From our results, it appears that the supernova blast adds more or less the same amount of momentum to the ISM independent of density if it occurs within a photoionized bubble, while some variance in the final momentum is caused by the momentum in the shell around the ionization front prior to the supernova. Our results (without photoionization or winds) agree well with the radial expansion of the supernova remnant found in Cioffi et al. (1988) and the energies in Thornton et al. (1998), but our momentum values are somewhat lower than the expressions given by Cioffi et al. (1988). We posit that this is due to simplifications made by their analytic function and more efficient cooling in our simulations. By contrast, we report good agreement with Walch & Naab (2014), who do include photoionization, despite differences in our simulation setups, suggesting that for a single star 10^{44} g cm s^{-1} is a good estimate of the momentum adds to the ISM a solar-metallicity star. In appendix A, we provide lists of numerical values from our simulation. This seems to suggest that while the structure of the remnant is sensitive to the physical model used and the initial conditions, the final momentum added to the ISM is more robust to changes in the simulation setup. However, neither of these works includes a turbulent ISM, which could become important in modelling the propagation of shocks from stars.

Turbulence in the remnant, approximated as the energy in non-radial flows, is calculated to be around 1 per cent of the kinetic energy and 10 per cent of the momentum, depending on the density and metallicity of the gas around the star. We thus do not expect a great deal of divergence between our 3D work and a 1D spherically-symmetric simulation with the same initial conditions. However, without doing the 3D experiment we cannot be sure that 1D spherically-symmetric simulations would be sufficient for modelling the explosions of stars of different stellar masses, which could seed larger instabilities and therefore give rise to more turbulence. For more realistic environments containing turbulent, multiphase fluid, self-consistent star formation and a galactic disc structure, the spherically-symmetric approximation breaks down and 3D simulations become unavoidable. We discuss some implications of this below.

There are a number of limitations to this work that should be considered. For one thing, we only simulate one star (albeit at two metallicities), rather than multiple stellar masses across the full IMFfrom 8 $M_\odot$ upwards. The wind luminosities and spectra of massive stars vary greatly depending on their initial mass, metallicity and rotation period, as well as multiplicity for the case of interacting binaries. Supernova energies for the most massive stars are either much larger or much smaller than the fiducial 10^{51} erg (Nomoto et al. 2003). Another consideration is whether supernovae add more momentum and energy to the ISM when they explode as part of a superwind, in which a succession of supernovae drives the expansion of a superbubble. This suggestion has recently been explored in models by (Keller et al. 2014; Sharma et al. 2014), who find substantial differences compared to results using isolated supernovae.

The environment around the star is also more complex than the uniform medium modelled in our work. It is not clear whether supernovae are more likely to explode in denser environments, in which stars are formed and which can live longer than the massive stars that form in them (Hennebelle & Falgarone 2012), or more diffuse environments that make up most of the ISM by volume. In addition to being multiphase, the ISM is turbulent, which adds an effective pressure to the medium that resists propagating stellar shocks (Raga et al. 2012). Recent simulations by Tremblin et al. (2014) seek to address this by simulating ionization fronts in both 1D and 3D in the presence of turbulence. As stated in the Introduction, there may be a case for including radiation pressure in future work. Stellar motions with respect to the ISM, not covered in this work, can also lead to features such as bow shocks. Magnetic fields and thermal conduction can also play a role in the ISM, although in our simple near-spherical setup magnetic fields are not expected to have a great effect (see, for example, Chevalier 1974), while conduction at the Field criterion requires a much higher resolution than that available in our runs. Various of these outstanding issues will be addressed in future works.

ACKNOWLEDGEMENTS

We would like to thank Philipp Podsiadlowski, Yohan Dubois and Patrick Hennebelle for useful comments and discussions during the writing of this paper, as well as the anonymous referee for suggested improvements to the text. We warmly thank Jonathan Patterson for his help in producing the results in this paper. The simulations presented here were run primarily on the DiRAC facility jointly funded by STFC, the Large Facilities Capital Fund of BIS and the University of Oxford. Additional simulations were run on the CC-IN2P3 Computing Center (Lyon/Villeurbanne – France), a partnership between CNRS/IN2P3 and CEA/DSM/Irfu.SG has received funding from a Cosmocomp fellowship and the European Research Council under the European Community's Seventh Framework Programme (FP7/2007-2013 Grant Agreement Nos 306483 and 291294). JR is funded by the European Research Council under the European Unions Seventh Framework Programme (FP7/2007-2013) / ERC Grant agreement 278594-GasAroundGalaxies, and the Marie Curie Training Network CosmoComp (PITN-GA-2009-238356). JB acknowledges support from the ANR BINGO project (ANR-08-BLAN-0316-01). JD and AS's research is supported by funding from Adrian Beecroft, the Oxford Martin School and the STFC.

REFERENCES

Agertz O., Kravtsov A. V., Leitner S. N., Gnedin N. Y., 2013, ApJ, 770, 25
Arthur S. J., Henney W. J., Mellema G., De Colle F., Vázquez-Semadeni E., 2011, MNRAS, 414, 1747
Avedisova V. S., 1972, SvA, 15, 708
Bate M. R., 2012, MNRAS, 419, 3115
Benson A. J., Bower R. G., Frenk C. S., Lacey C. G., Baugh C. M., Cole S., 2003, ApJ, 599, 38
Castor J., Weaver R., McCray R., 1975, ApJ, 200, L107
Ceverino D., Klypin A., 2009, ApJ, 695, 292
Chabrier G., 2003, PASP, 115, 763
Chevalier R. A., 1974, ApJ, 188, 501
Chevalier R. A., 1977, ARA&A, 15, 175
Chevalier R. A., 1982, ApJ, 258, 790
Chieffi A., Limongi M., 2013, ApJ, 764, 21
Chu Y.-H., Kennicutt R. C., 1994, ApJ, 425, 720
Cioffi D. F., McKee C. F., Bertschinger E., 1988, ApJ, 334, 252
Cox D. P., 1972, ApJ, 178, 159
Dale J. E., Bonnell I. A., Clarke C. J., Bate M. R., 2005, MNRAS, 358, 291
Dale J. E., Ngoumou J., Ercolano B., Bonnell I. A., 2014, MNRAS, 442, 694
Draine B. T., 2011, Physics of the Interstellar and Intergalactic Medium. Princeton Univ. Press, Princeton, NJ
Dubois Y., Teyssier R., 2008, A&A, 482, L13
Durier F., Dalla Vecchia C., 2012, MNRAS, 419, 465
Dwarkadas V. V., 2007, ApJ, 667, 226
Fraschetti F., Teyssier R., Ballet J., Decourchelle A., 2010, A&A, 515, A104
Garcia-Segura G., Langer N., Rozyczka M., Franco J., 1999, ApJ, 517, 767
Gerritsen J. P. E., Icke V., 1997, A&A, 325, 972
Gull S. F., 1973, MNRAS, 161, 47
Haardt F., Madau P., 1996, ApJ, 461, 20
Heger A., Fryer C. L., Woosley S. E., Langer N., Hartmann D. H., 2003, ApJ, 591, 288
Hennebelle P., Falgarone E., 2012, A&AR, 20, 55
Hennebelle P., Iffrig O., 2014, A&A, 570, A81
Hopkins P. F., Keres D., Onorbe J., Faucher-Giguere C.-A., Quataert E., Murray N., Bullock J. S., 2013, 19
Iffrig O., Hennebelle P., 2014, preprint (arXiv:1410.7972)
Kahn F. D., 1954, Bull. Astron. Inst. Neth., 12
Keller B. W., Wadsley J., Benincasa S. M., Couchman H. M. P., 2014, 13
Kimm T., Cen R., 2014, ApJ, 788, 121
Kovetz A., Yaron O., Prialnik D., 2009, MNRAS, 395, 1857
Koyama H., Inutsuka S.-i., 2004, ApJ, 602, L25
Krause M., Fierlinger K., Diehl R., Burkert A., Voss R., Ziegler U., 2012
Kroupa P., Weidner C., 2003, ApJ, 598, 1076
Krumholz M. R., 2014, preprint (arXiv:1402.0867)
Krumholz M. R., Matzner C. D., 2009, ApJ, 703, 1352
Krumholz M. R., Thompson T. A., 2012, ApJ, 760, 155
Kudritzki R.-P., Puls J., 2000, ARA&A, 38, 613
Leitherer C. et al., 1999, ApJS, 123, 3
McKee C. F., Ostriker J. P., 1977, ApJ, 218, 148

Mackey J., Gvaramadze V. V., Mohamed S., Langer N., 2015, A&A, 573, A10

Marigo P., Girardi L., Bressan A., Groenewegen M. A. T., Silva L., Granato G. L., 2008, A&A, 482, 883

Martizzi D., Faucher-Giguère C.-A., Quataert E., 2014, preprint (arXiv:1409.4425)

Mihos J. C., Hernquist L., 1994, ApJ, 437, 611

Murante G., Monaco P., Giovalli M., Borgani S., Diaferio A., 2010, MNRAS, 405, 1491

Navarro J., White S., 1993, MNRAS, 265, 271

Nomoto K., Maeda K., Mazzali P. A., Umeda H., Deng J., Iwamoto K., 2003, preprint (astro-ph/0308136)

Ntormousi E., Burkert A., Fierlinger K., Heitsch F., 2011, ApJ, 731, 13

Oort J. H., Spitzer L., 1955, ApJ, 121, 6

Raga A. C., Canto J., Rodriguez L. F., 2012, MNRAS, 419, L39

Redman M. P., Al-Mostafa Z. A., Meaburn J., Bryce M., 2003, MNRAS, 344, 741

Ricotti M., 2014, MNRAS, 437, 371

Rosdahl J., Blaizot J., Aubert D., Stranex T., Teyssier R., 2013, MNRAS, 436, 2188

Rozyczka M., Tenorio-Tagle G., Franco J., Bodenheimer P., 1993, MNRAS, 261, 674

Runacres M. C., Owocki S. P., 2005, A&A, 429, 323

Sales L. V., Marinacci F., Springel V., Petkova M., 2014, MNRAS, 439, 2990

Salpeter E. E., 1955, ApJ, 121, 161

Scannapieco C., Wadepuhl M., Parry O. H., Al E., 2012, MNRAS, 423, 1726

Sedov L. I., 1946, J. Appl. Math. Mech., 10, 241

Sharma P., Roy A., Nath B. B., Shchekinov Y., 2014, MNRAS, 443, 3463

Slyz A. D., Devriendt J. E. G., Bryan G., Silk J., 2005, MNRAS, 356, 737

Smartt S. J., Eldridge J. J., Crockett R. M., Maund J. R., 2009, MNRAS, 395, 1409

Spitzer L., 1978, Physical Processes in the Interstellar Medium. Wiley, New York

Springel V., Hernquist L., 2003, MNRAS, 339, 289

Strömgren B., 1939, ApJ, 89, 526

Tang S., Wang Q. D., 2005, ApJ, 628, 205

Tenorio-Tagle G., Bodenheimer P., Franco J., Rozyczka M., 1990, MNRAS, 244, 563

Tenorio-Tagle G., Rozyczka M., Franco J., Bodenheimer P., 1991, MNRAS, 251, 318

Teyssier R., 2002, A&A, 385, 337

Thornton K., Gaudlitz M., Janka H.-T., Steinmetz M., 1998, ApJ, 500, 95

Tremblin P., Schneider N., Minier V., Didelon P., Hill T., Others A., 2014, A&A, 564, A106

van Marle A. J., Langer N., Yoon S.-C., García-Segura G., 2008, A&A, 478, 769

Veilleux S., Cecil G., Bland-Hawthorn J., 2005, ARA&A, 43, 769

Vishniac E. T., 1983, ApJ, 274, 152

Vishniac E. T., 1994, ApJ, 428, 186

Walch S. K., Naab T., 2014, preprint (arXiv:1410.0011)

Walch S. K., Whitworth A. P., Bisbas T., Wünsch R., Hubber D., 2012, MNRAS, 427, 625

Walch S., Whitworth A. P., Bisbas T. G., Wunsch R., Hubber D. A., 2013, MNRAS, 435, 917

Weaver R., McCray R., Castor J., Shapiro P., Moore R., 1977, ApJ, 218, 377

APPENDIX A: TABULATED ENERGIES AND MOMENTA

In this appendix, we include sampled values for the energies and momenta in each run. In Tables A1 and A2, we give values for each of the runs at 0.1 and 30 atoms cm^{-3} that include a supernova only, a supernova and stellar winds, a supernova and photoionization, and all three processes. In Tables A3 and A4, we give values for all runs

Table A1. Table of energies and momenta calculated from each simulation in the runs at 0.1 and 30 atoms cm^{-3} 2 Myr after the supernova. As in Thornton et al. (1998), 'R' refers to the remnant, i.e. the whole structure around the star, 'S' refers to the shell, and 'B' refers to the hot bubble. The subscripts 'tot', 'kin', 'th' and 'turb' refer, respectively, to the total, kinetic, thermal and turbulent energy. All energy values are in $\log_{10}$(erg). The subscripts 'mom,bulk' and 'mom,turb' refer to the bulk momentum and the momentum in turbulent flows, respectively. All momentum values are in $\log_{10}$(g cm s^{-1}).

Runs	$R_{\rm tot}$	$R_{\rm kin}$	$R_{\rm th}$	$R_{\rm turb}$	$S_{\rm kin}$	$B_{\rm th}$	$S_{\rm mom,bulk}$	$S_{\rm mom,turb}$
N0.1ZsoS	49.624	49.536	48.889	47.800	49.519	48.133	43.673	42.759
N0.1ZsoSW	49.572	49.457	48.938	47.888	49.409	48.560	43.564	42.769
N0.1ZsoSR	50.027	49.685	49.764	47.327	49.678	49.704	44.024	42.675
N0.1ZsoSWR	50.037	49.687	49.780	47.955	49.678	49.715	44.013	43.040
N30ZsoS	48.607	48.556	47.654	46.223	48.508	46.165	43.339	42.188
N30ZsoSW	48.946	48.907	47.876	46.609	48.849	46.637	43.562	42.412
N30ZsoSR	49.264	49.209	48.344	47.137	49.188	47.855	43.979	42.887
N30ZsoSWR	49.324	49.269	48.398	47.299	49.249	47.962	44.015	42.974

Table A2. As for Table A1 but sampled at $t_{\rm f}$, which is defined as 13 times the time after the supernova at which the total luminosity from radiative cooling is at a maximum (see Thornton et al. 1998).

Runs	$t_{\rm f}$/Myr	$R_{\rm tot}$	$R_{\rm kin}$	$R_{\rm th}$	$R_{\rm turb}$	$S_{\rm kin}$	$B_{\rm th}$	$S_{\rm mom,bulk}$	$S_{\rm mom,turb}$
N0.1ZsoS	0.669	50.042	49.964	49.257	47.295	49.952	48.835	43.662	42.216
N0.1ZsoSW	0.144	50.590	49.973	50.470	48.439	49.938	50.451	43.445	42.461
N0.1ZsoSR	2.720	49.958	49.653	49.661	47.293	49.645	49.591	44.035	42.701
N0.1ZsoSWR	2.176	50.015	49.676	49.750	47.927	49.665	49.682	44.016	43.037
N30ZsoS	0.101	49.607	49.598	47.951	46.591	49.589	46.421	43.370	41.795
N30ZsoSW	0.108	49.911	49.659	49.556	47.991	49.597	49.536	43.558	42.666
N30ZsoSR	0.190	50.442	49.353	50.405	48.012	49.253	50.398	43.822	42.777
N30ZsoSWR	0.073	50.834	49.551	50.811	48.200	48.985	50.808	43.567	42.603

Table A3. Table of energies calculated from each simulation in the containing winds and photoionization runs 2 Myr after the supernova. Labels as in Table A1.

Runs	R_{tot}	R_{kin}	R_{th}	R_{turb}	S_{kin}	B_{th}	$S_{\mathrm{mom,bulk}}$	$S_{\mathrm{mom,turb}}$
N0.1ZSOSWR	50.037	49.687	49.780	47.955	49.678	49.715	44.013	43.040
N0.5ZSOSWR	49.771	49.470	49.470	47.525	49.454	49.401	43.959	42.869
N5ZSOSWR	49.571	49.435	49.000	47.000	49.416	48.883	44.031	42.725
N30ZSOSWR	49.324	49.269	48.398	47.299	49.249	47.962	44.015	42.974
N100ZSOSWR	49.152	49.103	48.184	46.964	49.091	47.282	43.971	42.848
N0.1ZLOSWR	50.253	49.595	50.145	46.134	49.525	50.054	44.074	42.060
N0.5ZLOSWR	49.929	49.374	49.787	46.251	49.323	49.697	44.039	42.180
N5ZLOSWR	49.502	49.099	49.284	46.224	49.073	49.157	44.000	42.396
N30ZLOSWR	49.084	48.653	48.882	46.295	48.623	48.701	43.819	42.516
N100ZLOSWR	48.858	48.416	48.664	45.923	48.392	48.397	43.743	42.380

Table A4. Table of energies calculated from each simulation in the containing winds and photoionization runs t_{f} after the supernova. t_{f} is defined by Thornton et al. (1998) as 13 times the time at which the total luminosity via radiative cooling is at maximum. Labels as in table A1.

Runs	t_{f}/Myr	R_{tot}	R_{kin}	R_{th}	R_{turb}	S_{kin}	B_{th}	$S_{\mathrm{mom,bulk}}$	$S_{\mathrm{mom,turb}}$
N0.1ZSOSWR	2.176	50.015	49.676	49.750	47.927	49.665	49.682	44.016	43.037
N0.5ZSOSWR	1.458	49.884	49.498	49.654	47.501	49.482	49.605	43.949	42.828
N5ZSOSWR	0.861	50.047	49.501	49.901	47.353	49.476	49.882	43.991	42.708
N30ZSOSWR	0.073	50.834	49.551	50.811	48.200	48.985	50.808	43.567	42.603
N100ZSOSWR	0.084	50.673	49.331	50.653	47.887	49.050	50.650	43.648	42.667
N0.1ZLOSWR	3.694	50.424	50.003	50.217	48.474	49.961	49.878	44.389	43.337
N0.5ZLOSWR	2.461	50.096	49.740	49.844	48.019	49.728	49.675	44.316	43.166
N5ZLOSWR	1.401	50.022	49.543	49.846	47.346	49.530	49.776	44.289	42.972
N30ZLOSWR	0.622	50.204	49.349	50.139	47.575	49.302	50.108	44.159	43.003
N100ZLOSWR	0.228	50.488	49.287	50.460	47.936	49.108	50.445	44.019	42.903

that include all three processes, varying according to density and metallicity in the external medium. Values are given at 2 Myr after the supernova, and at t_{f}. t_{f} is defined by Thornton et al. (1998) as 13 t_0, where t_0 is the time at which the luminosity from radiative cooling is at a maximum in the system as a whole. Unsurprisingly, the majority of the kinetic energy is in the shell. However, for late times the shell accounts for much of the thermal energy in the system, since the bubble has cooled rapidly from temperatures of $\sim 10^7$ K. By contrast, the high density of the shell allows it to retain a large amount of thermal energy even though its temperature is relatively low.

This paper has been typeset from a TEX/LATEX file prepared by the author.